Transition to Aperiodic Variability in a Wind-Driven Double-Gyre Circulation Model

KYUNG-IL CHANG

Marine Environment and Climate Change Laboratory, Korea Ocean Research and Development Institute, Ansan, Korea

MICHAEL GHIL* AND KAYO IDE

Department of Atmospheric Sciences and Institute of Geophysics and Planetary Physics, University of California, Los Angeles, Los Angeles, California

CHUNG-CHIENG AARON LAI

Earth and Environmental Sciences Division, Los Alamos National Laboratory, Los Alamos, New Mexico

(Manuscript received 15 March 2000, in final form 26 July 2000)

ABSTRACT

Multiple equilibria as well as periodic and aperiodic solution regimes are obtained in a barotropic model of the midlatitude ocean's double-gyre circulation. The model circulation is driven by a steady zonal wind profile that is symmetric with respect to the square basin's zonal axis of north–south symmetry, and dissipated by lateral friction.

As the intensity of the wind forcing increases, an antisymmetric double-gyre flow evolves through a pitchfork bifurcation into a pair of steady mirror-symmetric solutions in which either the subtropical or the subpolar gyre dominates. In either one of the two asymmetric solutions, a pair of intense recirculation vortices forms close to and on either side of the point where the two western boundary currents merge to form the eastward jet. To the east of this dipole, a spatially damped stationary wave arises, and an increase in the steady forcing amplifies the meander immediately to the east of the recirculating vortices. During this process, the transport of the weaker gyre remains nearly constant while the transport of the stronger gyre increases.

For even stronger forcing, the two steady solution branches undergo Hopf bifurcation, and each asymmetric solution gives rise to an oscillatory mode, whose *subannual* period is of 3.5–6 months. These two modes are also mirror-symmetric in space. The time-average difference in transport between the stronger and the weaker gyre is reduced as the forcing increases further, while the weaker gyre tends to oscillate with larger amplitude than the stronger gyre. Once the average strength of the weaker gyre on each branch equals the stronger gyre's, the solution becomes aperiodic. The transition of aperiodic flow occurs through a global bifurcation that involves a homoclinic orbit. The subannual oscillations persist and stay fairly regular in the aperiodic solution regime, but they alternate now with a new and highly energetic, *interannual* oscillation. The physical causes of these two oscillations—as well as of a third, 19-day oscillation—are discussed. During episodes of the high-amplitude, interannual oscillation, the solution exhibits phases of either the subtropical or subpolar gyre being dominant. Even lower-frequency, interdecadal variability arises due to an irregular alternation between subannual and interannual modes of oscillation.

1. Introduction and motivation

Western boundary currents and their extension into the ocean's interior as a detached zonal jet exhibit high temporal variability (Fu and Smith 1996). The eddy kinetic energy distribution determined by long-term ship drift and satellite-tracked drifter data shows a maximum of variability in the western part of the midlatitude ocean basins, along the western boundary currents and their extension (Wyrtki et al. 1976; Brugge 1995). Various observations, though limited in spatial and temporal coverage, suggest the existence of distinct scales of temporal variability in these currents—from subannual (e.g., Lee and Cornillon 1996) through seasonal (e.g., Ichikawa and Beardsley 1993; Schott and Molinari 1996) and interannual (e.g., Mizuno and White 1983;

* Additional affiliation: Laboratoire de Météorologie Dynamique du CNRS, Ecole Normale Supérieure, Paris, France.

Corresponding author address: Dr. Kyung-Il Chang, Marine Environment and Climate Change Laboratory, Korea Ocean Research and Development Institute, Ansan, P.O. Box 29, 425-600 Seoul, Korea.
E-mail: kichang@kordi.re.kr

Auer 1987), and all the way to interdecadal (e.g., Deser et al. 1996).

This observed variability can be divided into two types: forced or external and free or internal variability. The former is the response to changes in the external forcing, especially in wind stress or buoyancy fluxes, while the latter is due to the system's intrinsic instability and nonlinearity. The forced variability does not always account for all or even most of the observed variability. For example, Niiler and Richardson (1973) noted a discrepancy between the observed seasonal variability of the Florida Current transport and the corresponding Sverdrup transport. A number of recent modeling studies have suggested a new class of intrinsic-variability mechanisms of the wind-driven circulation as a possible source of observed low-frequency variability (Moro 1990; Jiang et al. 1995; Speich et al. 1995; Dijkstra and Katsman 1997; Berloff and Meacham 1997, 1998; Meacham and Berloff 1997a).

The theory of the wind-driven circulation is central to midlatitude physical oceanography. Linear, steady-state versions of the problem have been studied theoretically by Stommel (1948) and Munk (1950). Nonlinear, frictional versions of the problem have been studied in idealized basins by Bryan (1963) and Veronis (1966). The simplest formulation of the problem of interest here is to describe the steady, large-scale barotropic circulation of a closed, rectangular, flat-bottomed ocean basin on a rotating earth, driven by an idealized zonal wind and dissipated by either bottom friction or lateral friction. This simple system is governed by a nondimensionalized barotropic vorticity equation that contains two nondimensional parameters, the Ekman number and the Rossby number. Most of the classical studies of this problem concentrate on the dependence of its steady-state solution on these two parameters (e.g., Briggs 1980; Böning 1986).

In a nonlinear system, multiple equilibria may exist, and the system can undergo abrupt transitions from one equilibrium to another as parameters change. In the context of the wind-driven ocean circulation, Veronis (1963) was the first to examine multiple steady states and transitions between them in a single anticyclonic gyre. More recently, multiple equilibria and intrinsic low-frequency oscillations in the wind-driven, double-gyre system have been studied using a reduced-gravity shallow-water model (Jiang et al. 1995; Speich et al. 1995), a single-layer quasigeostrophic (QG) model (Cessi and Ierley 1995), a reduced-gravity QG model (McCalpin and Haidvogel 1996; Dijkstra and Katsman 1997), and a two-layer QG model (Dijkstra and Katsman 1997). Multiple steady states, including unstable ones, were found systematically in regions of a parameter space defined by the Ekman and Rossby numbers. This was the case in both wind-driven single-gyre (Ierley and Sheremet 1995; Sheremet et al. 1997) and double-gyre (Cessi and Ierley 1995; Jiang et al. 1995; Speich et al. 1995; Dijkstra and Katsman 1997) circulation models. In highly inertial cases (McCalpin and Haidvogel 1996), the multiple equilibria were replaced by multiple flow regimes, distinguished by their energy level.

In a double-gyre circulation forced by a meridionally symmetric zonal wind, the resulting circulation is antisymmetric when the system is weakly nonlinear. As the nonlinearity increases, the antisymmetric steady solution loses its stability to a pair of asymmetric solutions through a pitchfork bifurcation (Cessi and Ierley 1995; Dijkstra and Katsman 1997; Ghil et al. 2001, manuscript submitted to *Physica D*, hereafter GFS). Jiang et al. (1995) showed analytically how this occurs due to mirror symmetry in the governing QG potential vorticity equation. In this case, all solutions are either symmetric themselves about the symmetry axis of the domain and the forcing, or have a mirror-symmetric partner. Even when the governing equations or the forcing do not admit a perfect midbasin symmetry, a pair of asymmetric solutions that is nearly mirror symmetric arises through a perturbed pitchfork bifurcation (Jiang et al. 1995; Speich et al. 1995). The unstable steady antisymmetric solution exhibits a more intense double-gyre flow compared with that in either asymmetric solution (Cessi and Ierley 1995; Speich et al. 1995); that is, it is more energetic than the asymmetric solutions.

As the forcing is increased or the dissipation is reduced, either branch of asymmetric steady solutions loses in turn its stability to periodic motions that arise through a Hopf bifurcation (Jiang et al. 1995; Speich et al. 1995; Dijkstra and Katsman 1997). In the double-gyre problem, the periodic flows that emanate from one of the two solution branches can have a different timescale than for the other (Jiang et al. 1995; Speich et al. 1995; Dijkstra and Katsman 1997). In the 1.5-layer shallow-water model, periodic solutions that bifurcate off the branch that has a stronger subtropical gyre have an interannual period, while the period is subannual for the other branch, along which the subpolar gyre is stronger (Speich et al. 1995). The same two distinct temporal scales of oscillation also occur in a 1.5-layer QG model, for which full midbasin symmetry prevails (Dijkstra and Katsman 1997).

As the forcing is increased further or the dissipation decreased even more, the flow becomes more intense, the nonlinear effects more important, especially near the western boundary and the jet separation, and the solution eventually becomes aperiodic. In the case of the single-gyre circulation, this transition occurs via quasiperiodic motions (Berloff and Meacham 1997, 1998; Meacham and Berloff 1997a). Power spectra of the quasiperiodic motions involve discrete peaks at two or more incommensurable frequencies, often superimposed on a low level of background noise. The spectral power at lower, interannual and interdecadal frequencies increases substantially for chaotic motions.

In many bifurcation studies of geophysical flows (Ghil and Childress 1987) it has been observed that the periodic solutions that constitute but one signpost on

the ''route to chaos'' leave their spectral imprint on the chaotic motions that prevail further on along this successive-bifurcation route. Furthermore, the spatiotemporal patterns associated with the instability mechanism that gives rise to the Hopf bifurcation are often still discernible in the chaotic evolution (Ghil and Robertson 2000).

The wind-driven circulation in a double-gyre ocean basin also becomes aperiodic above a certain threshold of nonlinearity (Jiang et al. 1995; Speich et al. 1995). The spectrum of an aperiodic shallow-water solution calculated for a rectangular basin close in size to the North Atlantic is dominated by interannual peaks at well-separated frequencies, which also contain the frequency of the original Hopf bifurcations (Speich et al. 1995). In the aperiodic regime explored by McCalpin and Haidvogel (1996), three maxima appear in a histogram of their QG model's kinetic energy; they correspond to a high, a low, and an intermediate energy level. The high-energy regime is characterized by a long penetration scale of the zonal jet, little meandering, and limited eddy activity. The low-energy regime is characterized by a short jet penetration, substantial meandering, and increased eddy activity. The low-energy regime is preferred in these authors' simulations since their wind field lacks midbasin symmetry and thus favors a particular branch of the perturbed pitchfork bifurcation [see also Moro's (1990) results and Jiang et al.'s (1995) analysis of QG models]. The irregular transitions among these regimes result in the saturation of the model's power spectrum toward the lowest frequencies.

The above studies clearly show that, even when the wind stress is steady, the model ocean's circulation can exhibit internal variability on various timescales. In the double-gyre models, whether QG or shallow water, single or multilayer, the variability is concentrated spatially where the flow is most intense, near the confluence of the two counterrotating gyre western boundary currents, and their separation and eastward extension (Jiang et al. 1995; Speich et al. 1995; Dijkstra and Katsman 1997). This feature resembles at least qualitatively the observations (e.g., Brugge 1995; Fu and Smith 1996). The model results so far lack realism in several respects, and it is not yet known how much the intrinsic variability they exhibit contributes to observed oceanic variability. Still, nonlinear dynamics clearly affects the variability of the midlatitude oceans, especially that of the western boundary currents and eastward jets. Speich et al.'s (1995) comparison of simulated and observed spectra, in particular, strongly suggests that the internal variability of their simulated midlatitude ocean is an important factor in the observed interannual variability of the North Atlantic.

The idealized model studies so far have not clarified how the aperiodic low-frequency variability arises in a double-gyre configuration from the periodic solutions. Indeed, most of these studies used a global quantity like the total kinetic or potential energy in analyzing aperiodic-regime results and did not examine the detailed dynamics of the transition to this regime or within it. The aperiodic variability seems to arise mostly from the interaction between the intense subtropical and subpolar vortices. The purpose of this paper is to revisit the double-gyre wind-driven barotropic circulation of a flat-bottomed ocean in order to gain more insight into the system's successive bifurcations. It emphasizes the transition to aperiodic solutions, as well as describing and explaining the internal variability of the latter. To do so, we study a barotropic numerical model in a square ocean basin and examine systematically the changes in the wind-driven double-gyre circulation as the Rossby number changes.

The paper is structured as follows. Section 2 describes the idealized model used in the study together with its finite difference discretization. The barotropic vorticity equation is presented in nondimensional form in section 2a. This form is used in section 2b to choose the parameters that we change systematically to examine the evolution of the numerical solutions. The dependence of these solutions on a chosen parameter—and their physical nature—is considered next, with steady-state solutions and the overall bifurcation structure presented in section 3 and time-dependent solutions in section 4. Concluding remarks appear in section 5.

2. The numerical model

a. Governing equations and discretization

The numerical model employed in this study is a barotropic version of the semi spectral primitive-equation model (SPEM) of Haidvogel et al. (1991a). These authors and Hedstrom (1994) give a complete description of SPEM and its solution procedure. The SPEM solves the fully nonlinear primitive equations of motion using the hydrostatic, rigid-lid, and Boussinesq approximations. The model equations are discretized by finite differences in the horizontal; the spectral expansion in the vertical uses modified Chebyshev polynomials as basis functions. Model variables are arranged on a staggered Arakawa C-grid in the horizontal, and a centered, second-order finite difference approximation is adopted. Applications of SPEM to physical oceanographic studies can be found in Gawarkiewicz and Chapman (1991), Haidvogel et al. (1991b), and Chen et al. (1996).

In the present paper, we only consider a barotropic version of the SPEM model. In a companion paper, however, we exploit more fully the flexibility of SPEM with respect to variable bottom topography, as we explore the effect of marginal seas on the double-gyre circulation. The barotropic vorticity equation (BVE) in a rectangular basin governs the dynamics of the system that we explore,

$$(\nabla^2\psi)_t + J(\psi, \nabla^2\psi) + \beta\psi_x = -(1/H)\tau^x_y/\rho_0 + A_h\nabla^4\psi, \quad (1)$$

where H is the basin's constant depth, β is the meridional gradient of the Coriolis parameter, τ^x is the zonal component of the wind stress, ρ_0 is the water's constant density, A_h is the horizontal viscosity, J is the Jacobian operator, ∇^2 and ∇^4 are the Laplacian and biharmonic operators, and subscripts (x, y, t) denote partial differentiation with respect to the corresponding variables. The BVE governs the streamfunction ψ for the vertically averaged velocity components $u = -\psi_y$, $v = \psi_x$. The wind stress is assumed to have a simple symmetric form,

$$\tau^x = -T_0 \cos(2\pi y/L_y), \tag{2}$$

where T_0 is its amplitude and L_y is the basin width in the y direction; we use $L_x = L_y$ for simplicity. The wind stress is applied as a body force to the present barotropic model's single layer.

The forced–dissipative BVE is nondimensionalized by the scaling

$$(x, y) = L(x^*, y^*), \qquad t = (\beta L)^{-1} t^*, \qquad \tau = T_0 \tau^*,$$
$$\psi = 2\pi T_0/(\beta H \rho_0)\psi^*, \tag{3}$$

where the asterisks denote the scaled variables. This scaling yields

$$(\nabla^2\psi)_t + RJ(\psi, \nabla^2\psi) + \psi_x = -\sin(2\pi y) + E_L\nabla^4\psi, \tag{4}$$

where all the variables are now nondimensional and the asterisks have been dropped. The streamfunction is scaled by the basin's maximum possible Sverdrup transport.

The forward-integration method adopted in SPEM is similar to that of other ocean general circulation models (GCMs). The total velocity components are decomposed into an external, vertically averaged mode plus internal modes. The vertically averaged velocity field is determined by time stepping of the BVE, and the corresponding values of the streamfunction field are determined from the associated elliptic equation. The internal velocity field in the present barotropic configuration—with constant density and wind forcing of body-force type—is zero. The BVE in a flat-bottomed rectangular ocean basin is symmetric when the applied wind stress curl admits the same symmetry about an eastward-pointing axis, as is the case for Eq. (2). The SPEM vorticity equation (1) differs slightly from that given by the QG approximation in the form of the forcing term. The symmetry, however, is not violated when the forcing is given as in the nondimensional Eq. (4).

b. Choice of parameters

Two nondimensional numbers arise in Eq. (3), the Rossby number R and the horizontal Ekman number E_L,

$$R = 2\pi T_0/(\rho_0 \beta^2 H L^3), \tag{5a}$$

$$E_L = A_h/(\beta L^3). \tag{5b}$$

TABLE 1. Model parameters.

Parameter	Value
Coriolis parameter, $f = f_0 + \beta y$	$f_0 = 9.3744 \times 10^{-5}$ s^{-1} (40°N) $\beta = 2 \times 10^{-11}$ m^{-1}s^{-1}
Viscosity coefficient	$A_h = 5000$ m^{2}s^{-1}
Ocean depth	$H = 400$ m
Domain extent	$L_x = L_y = 2560$ km
Grid resolution	$\Delta x = \Delta y = 20$ km
Time step	$\Delta t = 40$ min

With these definitions, the nondimensional widths δ_I and δ_M of the inertial and frictional boundary layers, respectively, become

$$\delta_I = R^{1/2}, \qquad \delta_M = E_L^{1/3}. \tag{6a,b}$$

Oceanographically relevant values of these widths are $0 < \delta_I, \delta_M \leq 0.1$ (e.g., Sheremet et al. 1997).

The model domain is a closed rectangular basin with a flat bottom. Free-slip lateral boundary conditions were applied. Table 1 shows the parameter values used in our numerical experiments. The most important idealization in the present model study is the neglect of vertical stratification, and hence of baroclinic phenomena [compare Berloff and Meacham (1997, 1998), Dijkstra and Katsman (1997), and GFS, where the latter are present]. The total density was set equal to the constant value of $\rho_0 = 1000$ kg m^{-3}. The uniform ocean depth, H, was taken to be 400 m, which can be regarded as the mean depth of the permanent thermocline.

The details of the western boundary layer structure are thought to play an important role in determining the flow patterns obtained (e.g., Böning 1986). The dimensional length scale of the frictional Munk layer is $(A_h/\beta)^{1/3} \approx 63$ km. We choose, following Jiang et al. (1995) and Speich et al. (1995), $\Delta x = \Delta y = 20$ km. This permits a fairly good resolution of the Munk layer. GFS and Simonnet (1998) discuss further the effect of grid size on resolving the inertial phenomena in the highly nonlinear parts of the flow field.

GFS consider the total number of mutually independent nondimensional parameters for various models of the double-gyre problem via an application of Buckingham's Π theorem (Barenblatt 1987). We shall concentrate here on studying our model's bifurcation structure as a function of the forcing parameter δ_I. The ratio BLR (see section 3a below) of the two nondimentional parameters δ_I and δ_M represents the relative importance of inertial and frictional effects.

In a series of numerical experiments, the parameter δ_M is held fixed, while δ_I is gradually varied. This is achieved by keeping A_h constant and changing the wind stress intensity T_0; such a variation is equivalent, according to Eqs. (5,6), to varying the Rossby number R while keeping the Ekman number E_L fixed.

3. Numerical results

a. Classification of solutions

Numerical continuation methods have been used by Cessi and Ierley (1995), Speich et al. (1995), Dijkstra and Katsman (1997), Primeau (1998), and Simonnet (1998) to follow steady-state solution branches of the double-gyre problem in both shallow-water and QG models. There are two reasons for not using such a method here: (i) the domain size we chose to explore is larger than that used by these previous investigators, while our resolution is the same or similar, hence the state vector is too large to apply comfortably numerical continuation, and (ii) our emphasis lies on following the bifurcation tree past periodic and all the way into chaotic solutions, as done by Jiang et al. (1995) and GFS. We have used therefore a method that represents a ''poor man's version'' of continuation for steady-state solutions, but also applies to following in considerable detail time-dependent, periodic and aperiodic solutions.

To do so, we have kept $\delta_M = 2.46 \times 10^{-2}$ fixed and have explored solutions in the range of δ_I between 1.08×10^{-2} and 2.22×10^{-2}, or from 0.44 to 0.90 in terms of the BLR between the two length scales, $\mathrm{BLR} = \delta_I/\delta_M$. The numerical model was integrated forward in time for a fixed BLR value until a statistical-equilibrium state was attained; this takes usually about 10^3 days. Four scalar quantities were saved at one-day intervals for further analysis. The basin's total kinetic energy BKE is defined here to be the sum of the kinetic energy values at each grid cell over the entire domain.

The maximum transport within the subtropical and the subpolar gyres is defined in terms of the maximum positive and the (algebraically) minimum negative value of the barotropic streamfunction, ψ_{tr} and ψ_{po}, respectively, so that $|\psi_{tr}| = +\psi_{tr}$ and $|\psi_{po}| = -\psi_{po}$. Each one of these measures the instantaneous strength of the respect gyre. The normalized transport difference TD between the two gyres, cyclonic and anticyclonic, is defined by

$$\mathrm{TD} = [|\psi_{po}| - |\psi_{tr}|]/\max(|\psi|). \tag{7}$$

The difference TD is used as a measure of a solution's symmetry with respect to the midbasin axis. If TD equals zero, the model's double-gyre circulation is antisymmetric, with counterrotating subtropical and subpolar gyres of equal strength. As the scalar quantity TD deviates from zero, the circulation becomes more asymmetric. If TD is positive, the subpolar transport is larger than the subtropical one. As we shall see, this is associated with a more intense recirculation vortex in the southwest corner of the subpolar gyre, a smaller spatial extent of the gyre as a whole, and an eastward jet that lies on average to the north of the latitude of vanishing wind stress curl. The opposite is the case for $\mathrm{TD} < 0$.

For a given BLR value, we verify that a solution reaches statistical equilibrium by checking the behavior of the four scalar time series just defined. Once the transients have died down and all four time series indicate that a statistical equilibrium has been reached, the solution in question is run long enough to be able to study it in detail. Next, a new numerical experiment is started, in which a larger BLR value is now imposed. To make sure—to the extent possible—that the next solution is on the same branch as the previous ones, the final state of the previous experiment is used as the initial state of the new one. This yields 17 consecutive runs in which BLR ranges from 0.44 to 0.90, as the wind stress intensity T_0 increases from 0.5 dyn cm^{-2} to 2.1 dyn cm^{-2} in increments of 0.1 dyn cm^{-2}; the first of these runs was started from a state of rest.

Figure 1 shows the results for the last 11 of these 17 runs as continuous time series of the transport ratio TD, basin kinetic energy BKE, and nondimensional maximum transports $|\psi_{po}|$ and ψ_{tr} of the subpolar and subtropical gyres (Figs. 1b–e). Only the final 50 yr out of the total 140-yr run carried out with BLR = 0.65 are shown; these 50 yr illustrate clearly the transition from a symmetric steady state, with TD = 0, to an asymmetric one, with $\mathrm{TD} < 0$. The model was run for 90 yr using BLR = 0.9, the largest value, since the results indicated this value to be in the aperiodic regime, and we wished to accumulate a sufficiently long sample of flow patterns in this regime; only the first 30 yr are shown in the figure.

As BLR increases, we can discern essentially three types of solutions in Fig. 1: steady, between $t = 0$ and 120 yr; periodic, between $t = 120$ and roughly 175 yr; and aperiodic for $t \geq 175$ yr. The steady-state regime can be further divided into two subregimes: antisymmetric, when TD = 0, and asymmetric when $\mathrm{TD} \neq 0$ (see Fig. 1b).

The nonlinearity of the solutions can be measured by determining the ratio NR between the maximum transport $\psi_{\max}$ attained during a given run, $\psi_{\max} = \max(|\psi|)$, and the linear or Sverdrup transport

$$\psi_{\mathrm{Sv}} = 2\pi T_0/\beta\rho_0; \tag{8a}$$

thus

$$\mathrm{NR} = \psi_{\max}/\psi_{\mathrm{Sv}}. \tag{8b}$$

The ratio NR is plotted in Fig. 1a. For the aperiodic solution at BLR = 0.90, NR is greater than 2.5, and we truncate the plot there; clearly NR increases with BLR, and the solution becomes periodic when $\mathrm{NR} \geq 1.9$ and aperiodic when $\mathrm{NR} > 2.21$. For the given value of β (see Table 1) and the range of T_0 used here, the Sverdrup transport ranges between about 16 and 66 Sv (Sv $\equiv 10^6$ m^3 s^{-1}).

The role of NR here is similar to that of the maximum streamfunction value Q, normalized by the typical Sverdrup interior velocity, as used by Ierley and Sheremet (1995) and Sheremet et al. (1997) to characterize their multiple steady-state solutions in the single-gyre problem. In the present double-gyre problem, however, no ''inertial runaway'' of steady-state solutions (see Pedlosky 1996, and references therein) occurs. Instead, tran-

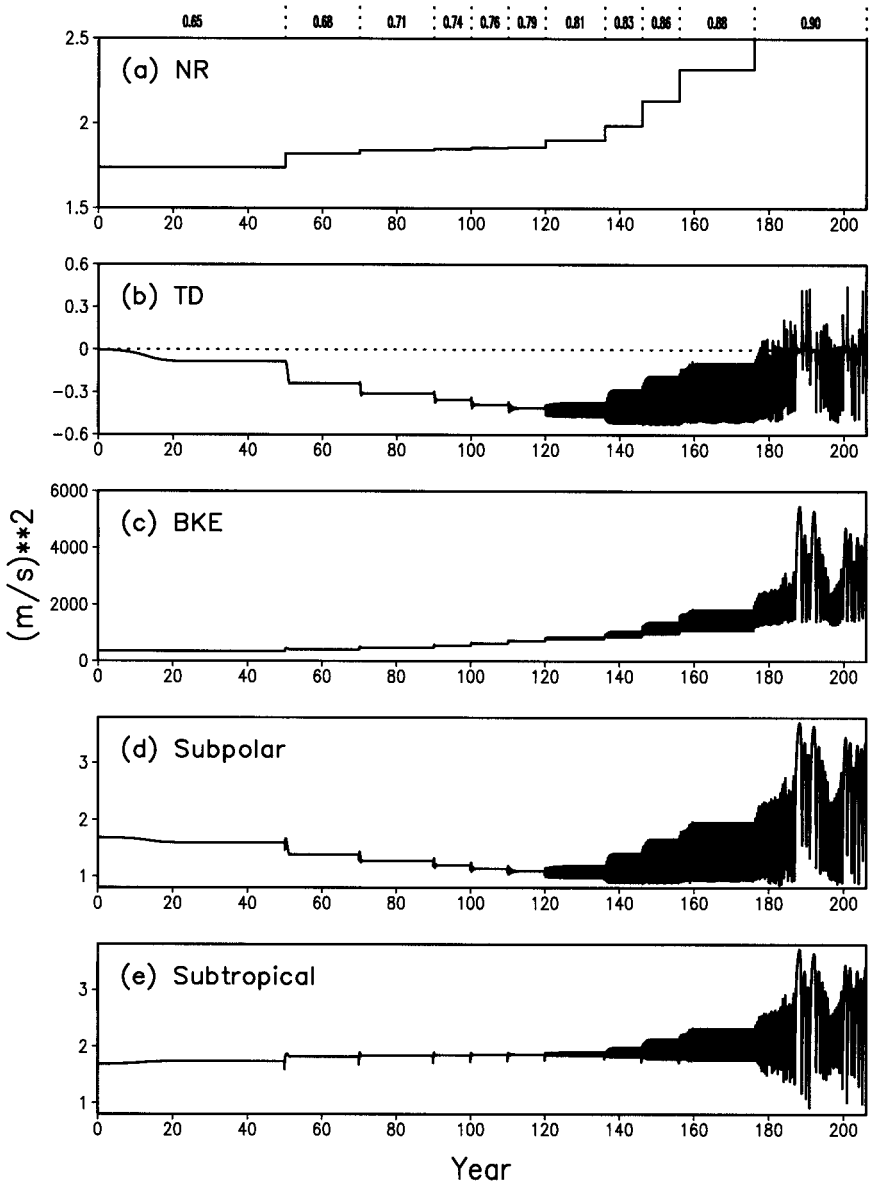

FIG. 1. A sequence of time series of (a) nonlinear transport ratio NR defined by Eq. (8) in the text, (b) normalized transport difference TD defined by Eq. (7) in the text, (c) basin kinetic energy BKE, (d) nondimensional maximum transport of the subpolar gyre, and (e) nondimensional maximum transport of the subtropical gyre. The five panels in the figure are based on 11 consecutive numerical experiments; the beginning and end of each experiment are marked by dotted lines on top of panel (a) and the values of BLR = δ_I/δ_M for each experiment are shown between the corresponding dotted lines.

sition to time-dependent solutions, periodic and aperiodic, takes place at reasonable values of NR [see also Jiang et al. (1995) and Speich et al. (1995) for similar results in a reduced-gravity, shallow-water model].

b. Pitchfork bifurcation

As the forcing increases from BLR = 0.44 to 0.62, the solutions stay antisymmetric, with TD = 0 (not shown in Fig. 1). Their flow patterns consist of two counterrotating gyres that are mirror images of each other in the problem's symmetry axis: the anticyclonic subtropical gyre and the cyclonic subpolar gyre have both equal strength and equal extent. The steady-state flow patterns at BLR = 0.52 and 0.62 are plotted in Figs. 2a and 2b, respectively. They show that a more and more intense recirculating vortex appears in the southwestern corner of the subpolar gyre and in the northwestern corner of the subtropical gyre, as the wind stress intensity T_0 and hence the nonlinearity of the

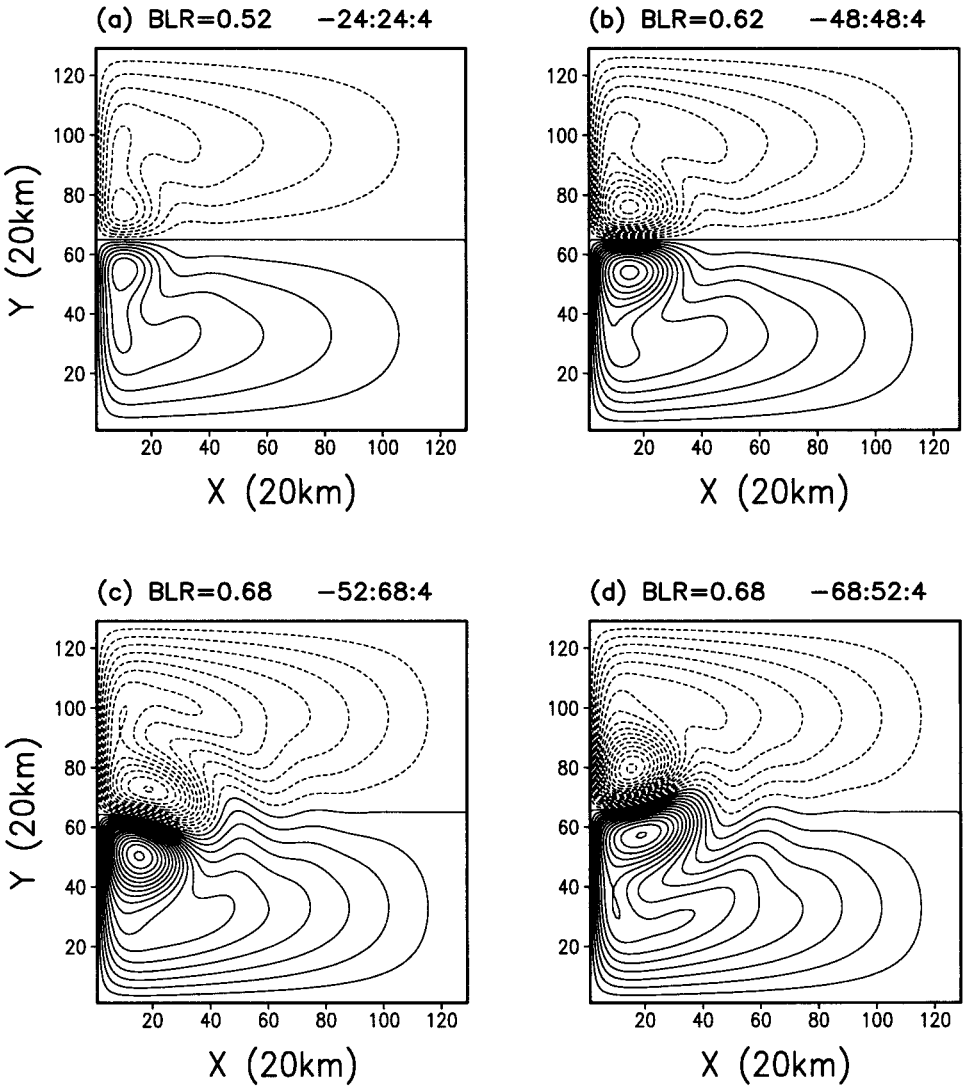

FIG. 2. Contour plots of streamfunction fields typical of steady-state solutions for antisymmetric solutions at (a) BLR = 0.52, and (b) BLR = 0.62 and for asymmetric solutions with pairwise mirror symmetry at BLR = 0.68 with (c) on the lower branch and (d) on the upper branch. Here and in all the following streamfunction plots, three numerals at the top right of each snapshot denote, in Sverdrup units (Sv $\equiv 10^6$ m^3 s^{-1}), the dimensional minimum and maximum ψ value for the contour lines, and the contour interval. Solid and dashed lines stand for positive and negative values, respectively.

solutions increases. The maximum negative and positive transport occur within these two vortices and exceed the Sverdrup value for the given wind stress by the ratio NR = 1.27 for BLR = 0.52 and NR = 1.58 for BLR = 0.62. Both vortices intensify to an equal degree as the forcing increases between BLR = 0.44 and 0.62, hence TD remains zero in this solution regime.

The TD value in Fig. 1b becomes negative when BLR increases from 0.62 to 0.65, which implies that the steady antisymmetric solution evolves into an asymmetric solution. The instability of the antisymmetric solution to asymmetric perturbations is still quite weak at this point, so we need to run the model for a long time in order to find a steady asymmetric solution at BLR = 0.65, starting from the antisymmetric solution at BLR = 0.62. The model was run for 140 yr and TD starts to deviate from zero only after 90 yr of integration (t = 0 in Fig. 1); hence only the final 50 yr of the run are shown in Fig. 1 for this BLR value. Once the asymmetric solution at BLR = 0.65 was obtained, we decreased the wind stress back to BLR = 0.62 and checked that the solution becomes antisymmetric again, which it does (not shown).

As BLR is increased further, the instability of the antisymmetric steady solution increases, and so does the asymmetry of the steady state to which the faster transient equilibrates. On the solution branch illustrated in Fig. 1, the asymmetric solution (Fig. 2c) is characterized

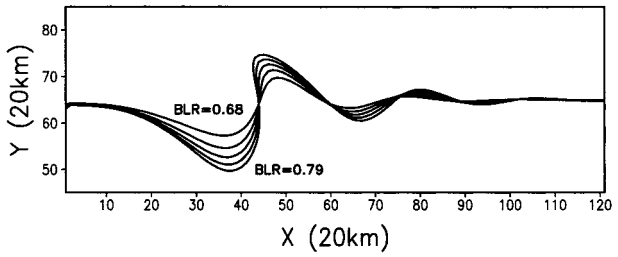

FIG. 3. Zero-streamline contours for five steady asymmetric solutions on the lower branch. The meanders east of the recirculation gyres increase in amplitude as the forcing is increased, while the wavelength remains the same.

by the subtropical gyre being stronger than the subpolar one. The subtropical and subpolar recirculation vortices form together an asymmetric dipole. Pulled by the stronger subtropical recirculation vortex, the subpolar gyre crosses the basin's zonal symmetry axis and wraps partially around the subtropical vortex's eastern flank. Steady asymmetric solutions are obtained in the BLR range from 0.65 to 0.79. The subtropical gyre transport increases within the range, while the subpolar gyre transport remains nearly constant (see Figs. 1d and 1e); this results in a further decrease of TD, as shown in Fig. 1b. Instead of gaining in strength, the subpolar recirculation vortex becomes more elongated in the NW–SE direction as BLR increases (see Fig. 3).

While the solution is antisymmetric, the separation points of the north- and south-flowing western boundary currents are also mirror images of each other. The eastward jet formed by their merging is fairly weak, since the solution is more frictional than inertial, and the jet strictly follows the midbasin symmetry axis. We shall use the zero contour of the barotropic streamfunction to define the axis of the eastward jet. The position of this contour line is plotted in Fig. 3 for five values of BLR between 0.68 and 0.79.

The jet's axis shows a spatially damped wave pattern, with a standing trough of largest amplitude located about 800 km east of the basin's western boundary and just to the east of the subtropical recirculation vortex. The ridge immediately downstream of this trough has a smaller amplitude, and the subsequently alternating troughs and ridges have smaller and smaller amplitudes. The characteristic wavelength of the meandering jet is of about 500–600 km. The entire wave pattern increases in amplitude with BLR: the nodal points stay fixed, while the steepness of the wave increases to the point where breaking seems to be imminent around the node located about 900 km east of the western boundary. This incipient wave breaking is clearly an inertial, nonlinear phenomenon; it may be the primary reason why the asymmetric steady state cannot be maintained as the forcing increases further and an oscillatory instability is triggered.

The common separation point of the two boundary currents, defined as the intersection of the zero streamline with the western boundary, occurs about 20 km (one grid point) south of the western boundary's midpoint, and its position does not change as the forcing increases (see Fig. 3). This constant location of the separation seems to be due to the use of free-slip boundary conditions. In a no-slip case like the one treated in detail by Jiang et al. (1995), the separation point was shifted southward by about 100 km in the asymmetric steady solutions and it changed substantially as the forcing increased. This allowed Jiang et al. to use the meridional position of the separation point to characterize their solutions, both steady and time dependent, and to construct their bifurcation diagram based on this scalar diagnostic. Further discussion of the role of the boundary conditions in the determination of the separation point can be found in Haidvogel et al. (1992) and in appendix A of Jiang et al. (1995).

The emergence of the symmetry-breaking solution branch herewith suggests that a pitchfork bifurcation occurs between BLR = 0.62 and 0.65. As discussed in section 1, the QG version of the double-gyre problem is perfectly mirror-symmetric when the wind stress and boundary conditions are; hence a pure pitchfork bifurcation arises as the wind forcing increases and leads to a pair of mirror-symmetric solutions, each of which is itself asymmetric. Multiple steady solutions at a fixed parameter value are thus possible. The other member of the asymmetric pair can be obtained using the QG symmetry (Cessi and Ierley 1995; Dijkstra and Katsman 1997). When the governing problem does not admit midbasin symmetry, a perturbed pitchfork bifurcation occurs and the other member of the pair can be found using a different initial state (Jiang et al. 1995). The lack of perfect mirror symmetry may be due to the form of the equations (shallow water or primitive equation rather than QG), the shape of the domain, or the forcing wind profile (Moro 1988). The physical mechanism of the symmetry breaking was analytically studied by Jiang et al. (1995).

As discussed in section 2a, our barotropic SPEM problem does have intrinsic midbasin symmetry. Still, as an additional check on the accuracy of our numerical procedures, we conducted experiments to verify the existence of the other member of the asymmetric pair of multiple solutions by taking an initial state

$$\psi_U(x, y, 0) = -\psi_L(x, -y, t_0),$$

where $\psi_L(x, y, t_0)$ is an asymmetric steady solution on the solution branch illustrated in Fig. 1. The model was then integrated for 5 yr with the initial state $\psi_U(x, y, 0)$ given above; this run showed virtually no changes between its initial state and the final, equilibrated solution. The other member of a mirror-symmetric pair of asymmetric solutions obtained at BLR = 0.68 by this procedure is also shown in Fig. 2d.

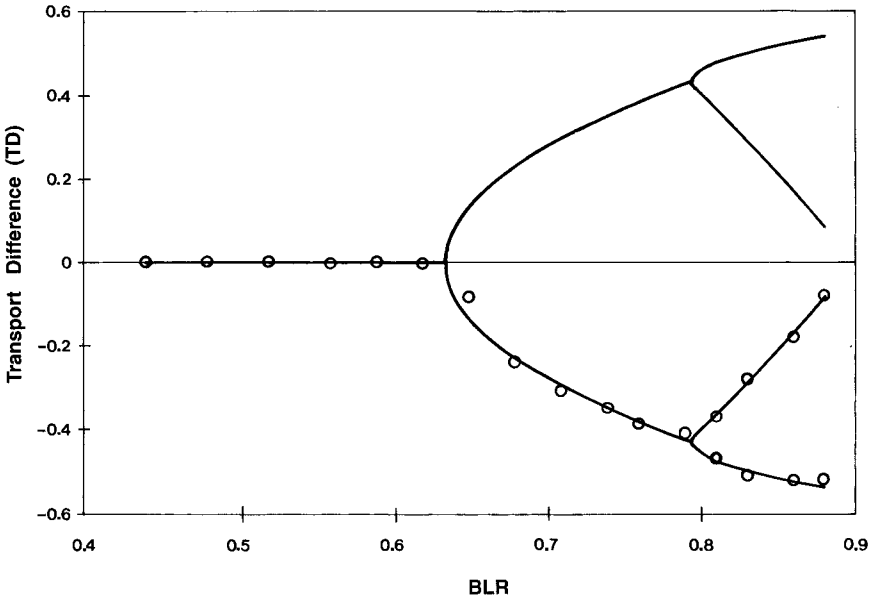

FIG. 4. Bifurcation diagram (heavy solid curves) based on TD values as a function of BLR, fitted by the least squares method to the points obtained numerically (open circles). Maximum and minimum values of TD are plotted for the periodic solutions that arise at BLR ≈ 0.80. Aperiodic solutions that arise for BLR = 0.90 on both branches are not shown.

c. Complete bifurcation diagram

As explained at the beginning of section 3a, the present problem exceeds the current capabilities of numerical continuation codes, with respect to the size of its state vector on the one hand, as well as the complexity of the solution branches that we wish to follow, on the other. The bifurcation diagram is constructed, therefore, based on the 17 numerical experiments with different BLR values, and using the run TD values as a function of BLR. In Fig. 4, a single TD value is plotted for the steady solutions, while (following Jiang et al. 1995) the maximum and minimum values are plotted for periodic solutions.

The normal form of a pitchfork bifurcation—in systems of both ordinary (e.g., Guckenheimer and Holmes 1983) and partial (e.g., Témam 1997) differential equations—involves a cubic nonlinearity, with the two mirror-symmetric branches forming a parabola that intersects the branch of antisymmetric solutions at right angles. Quon and Ghil (1992) applied this knowledge to obtain the bifurcation diagram of a highly resolved two-dimensional model of the thermohaline circulation. We follow them and least squares fit a parabola to the six pairs of points in the (TD–BLR) plane of Fig. 4 for $0.65 \leq \text{BLR} \leq 0.79$; it intersects the unique antisymmetric branch TD = 0 at BLR = 0.635, which is therewith our best approximation of the pitchfork bifurcation point.

Positive (negative) values on the ordinate of the TD versus BLR plot indicate that the subpolar (subtropical) gyre is stronger. We will refer, henceforth, to these as the upper (lower) branch of steady solutions. Asymmetric solutions on the upper (lower) branch have a more intense subpolar (subtropical) gyre and the eastward jet displaced northward (southward). This identification of the two branches is thus the same as in the bifurcation diagram of Jiang et al. (1995), who used the meridional position of the jet as their ordinate and another nondimensional measure of the forcing as their abscissa. The evolution of solutions shown in Fig. 1 corresponds to that on the lower branch.

Both stable and unstable steady solutions have been investigated by Newton's method in a wide region of the forcing versus dissipation plane for a single-gyre (Ierley and Sheremet 1995) as well as for a double-gyre (Cessi and Ierley 1995) barotropic circulation. Our choice of nondimensional parameters—$\delta_M = 2.46 \times 10^{-2}$, $1.08 \times 10^{-2} \leq \delta_I \leq 2.22 \times 10^{-2}$, with corresponding BLR values in the range $0.44 \leq \text{BLR} \leq 0.90$ — lies in the parameter region explored by Cessi and Ierley (1995), and our range for the coexistence of multiple stable equilibria is consistent with their results. An unstable antisymmetric solution exists within the same parameter range in a pitchfork bifurcation (Cessi and Ierley 1995; Speich et al. 1995; Dijkstra and Katsman 1997) but cannot be found by forward-marching numerical integration.

Multiple stable equilibria exist only in a fairly small portion of parameter space, for moderate-to-high forcing and moderate-to-low dissipation (see Cessi and Ierley 1995, Fig. 7; Jiang et al. 1995, Fig. 4). We consider only one value of δ_M here but can conjecture from these earlier studies that the pitchfork bifurcation point shifts to a lower (higher) value of δ_I as δ_M is decreased (in-

creased) in a (δ_I–δ_M) parameter plane. No multiple equilibria are found in highly inertial cases that correspond to very high forcing or very low dissipation (McCalpin and Haidvogel 1996; Meacham and Berloff 1997a).

Above BLR = 0.79, the steady solution branches lose their stability to periodic solutions through a Hopf bifurcation. In Fig. 1 it is clear that damped oscillations arise when changing BLR from 0.68 to 0.71 and so on; the oscillations become self-sustained at the transition from 0.79 to 0.81. The periodic solutions are found in a range of BLR from 0.81 to 0.88. The Hopf bifurcation is supercritical since (i) the finite amplitude of the periodic solution that appears at BLR = 0.81, immediately after the steady solution at BLR = 0.79, shrinks back to zero as BLR is decreased from 0.81 to 0.79 (not shown) and (ii) the amplitude of the periodic solutions after the Hopf bifurcation is a smoothly increasing function of BLR.

An increase in the oscillation amplitude with BLR is clearly apparent in Fig. 1. Figures 1d and 1e also indicate that the mean oscillation amplitude is larger in the subpolar transport on this lower branch, while the mean transport on it is larger for the subtropical gyre than the subpolar one. The opposite is true for solutions on the upper branch (not shown).

The normal form of a Hopf bifurcation has a quadratic right-hand side. Quon and Ghil (1995) and Chen and Ghil (1996) used this fact to least squares fit a parabola to the results of a limited number of numerical experiments, like the ones shown here in Fig. 4. This fit allowed them to obtain a good approximation of the bifurcation curve for thermohaline oscillations in a two-dimensional meridional-plane ocean model and a hybrid coupled ocean–atmosphere model, respectively; the latter had an idealized GCM at its ocean component (see also Ghil and Robertson 2000). We modify the procedure of these two earlier studies to account for the different amplitudes of the oscillations in the two-gyre respective transports: one branch of the ''skew parabola'' is scaled so that the two yield a symmetric parabola when doing the least squares fit. The intersection of the symmetrized parabola with the steady-solution branches yields the Hopf bifurcation point at BLR = 0.793 for both the upper and lower branch.

As BLR continues to increase, the periodic solutions on both branches lose their stability and aperiodic solutions arise eventually for BLR = 0.9 (Fig. 1). As noted before, the TD value in Fig. 1b decreases as BLR increases along the lower steady-solution branch. On the other hand, the mean TD value in the periodic-solution range increases as BLR increases along the continuation of this branch (see also lower half of Fig. 4) and its minima—in absolute value—eventually approach zero again (not shown in Fig. 4). Actually, the aperiodic solution arises after the fluctuations in TD touch the zero value; TD values become even positive intermittently for the aperiodic solution at BLR = 0.9 (see Fig. 1b). We will describe this transition to aperiodic solutions and the nature of these solutions in greater detail in section 4b below.

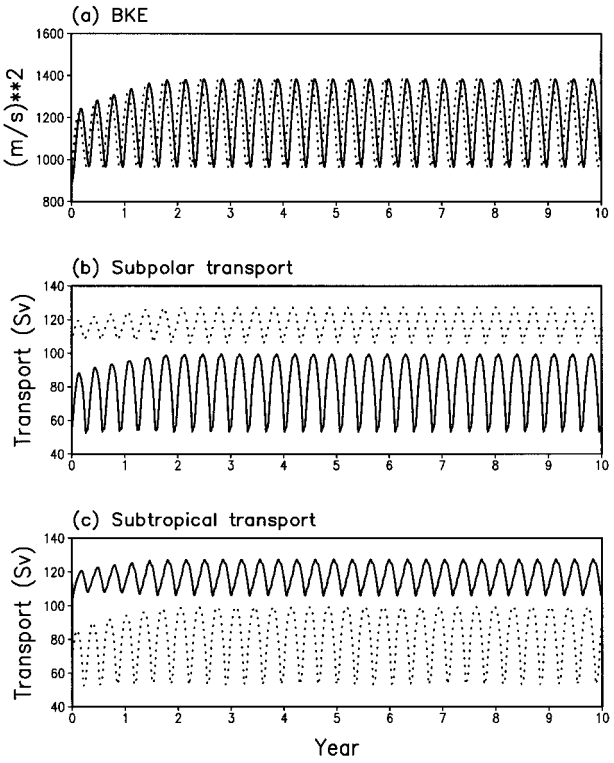

FIG. 5. Evolution in time of a periodic solution on the lower (solid lines) and upper (dotted lines) branches at BLR = 0.86. Plots of (a) basin kinetic energy BKE, (b) maximum transport of the subpolar gyre $|\psi_{po}|$, and (c) maximum transport of the subtropical gyre ψ_{tr}.

4. Time-dependent solutions

a. Periodic solutions

1) PHASE-SPACE AND SPATIOTEMPORAL ASPECTS

Periodic solutions with subannual periods arise by a Hopf bifurcation at BLR = 0.81 from the steady state. Figure 5 shows BKE and the maximum transports of the subpolar and subtropical gyres as a function of time for periodic solutions on the lower (solid line) and upper (dotted line) branches at BLR = 0.86. After a transient spinup of about 3 model years, the system clearly exhibits a purely periodic oscillation with a period of 126 days. Similar periods of 4–5 months have been found in an ocean GCM with North Atlantic basin bathymetry (C.-C. Ma, A. Wirth, K. Ide, C. R. Mechoso, and M. Ghil 1998, personal communication; see also Chassignet et al. 2000), as well as in a comparative study (Ide et al. 1997, unpublished manuscript) of TOPEX/Poseidon satellite altimetry data for the North Atlantic (Fu and Smith 1996) and of another GCM simulation (Chao et al. 1996) of this basin's variability.

On both branches, the oscillation's amplitude is higher in the weaker gyre than that in the stronger one. The

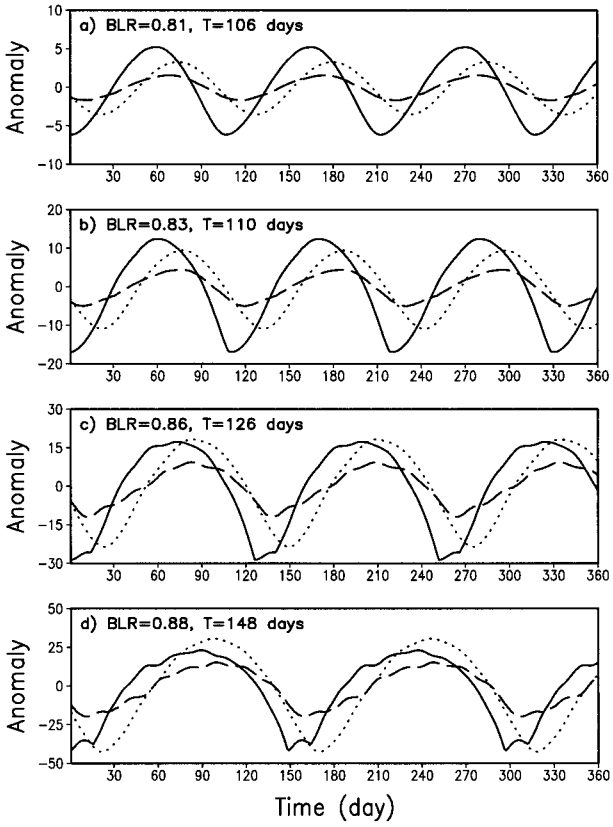

FIG. 6. Anomalies of the maximum subpolar transport $|\psi_{po}|$ (solid line), maximum subtropical transport ψ_{tr} (dashed line), and basin kinetic energy BKE (dotted line) for four periodic solutions on the lower branch. The anomalies are defined as the difference between the instantaneous values of a variable and its mean over the period; they are plotted at (a) BLR = 0.81, (b) BLR = 0.83, (c) BLR = 0.86, and (d) BLR = 0.88 for 1 yr after the system reaches an exactly periodic solution. The units on the ordinate are Sv for gyre transports and $10 \times m^2 s^{-2}$ for BKE, and T denotes the period of the oscillation.

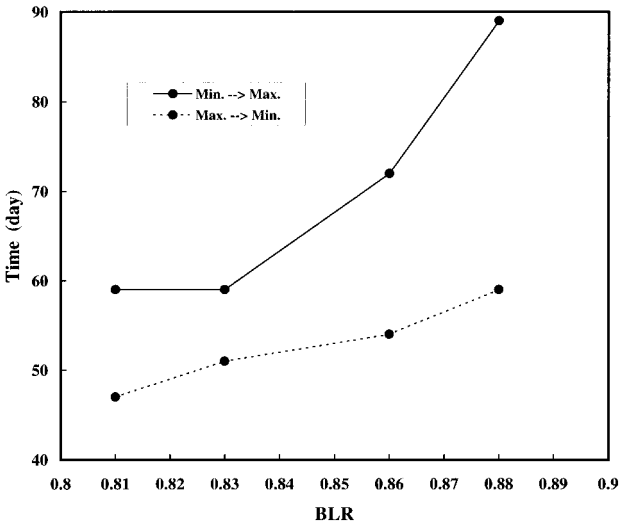

FIG. 7. The length of time over which the subpolar gyre transport $|\psi_{po}|$ reaches its maximum value from the minimum (solid line), and the minimum value from the maximum (dotted line) as a function of BLR. The four heavy dots indicate the data points for the four lower-branch periodic solutions shown in Fig. 6.

oscillatory modes on both branches have the same spatial mirror symmetry as the pairs of steady, asymmetric solutions. Anomalies of the subpolar ($|\psi_{po}|$, solid lines) and subtropical (ψ_{tr}, dashed lines) transports, and of BKE (dotted lines) as a function of time are shown in Fig. 6 for four periodic solutions at BLR = 0.81, 0.83, 0.86, and 0.88 on the lower branch. The anomalies are calculated by subtracting the instantaneous value from the mean value over one full period. Only one simulated year is shown for each solution, starting from the time when the subpolar gyre transport is at its minimum value, and after the asymptotic state of exact periodicity has been reached. The BKE is downscaled by a factor of 10^{-1}, in order to fit it into the same plot with the transports.

As BLR increases, the oscillation period increases from 106 days at BLR = 0.81 to 148 days at BLR = 0.88. On this lower branch, the oscillation amplitude of the weaker subpolar transport (solid) is larger than that of the stronger (on average) subtropical (dashed) as mentioned before. The changes in the subpolar gyre transport lead those in the subtropical gyre, which leads in turn the ones in BKE. In these periodic solutions, a slow buildup toward maximum transport is followed by a rapid decay toward minimum transport. This relaxation–oscillation behavior is somewhat less pronounced in BKE. As BLR increases and the system becomes more inertial, the length of time for either gyre to build up toward its maximum transport increases faster than the length of time for the transport to drop from this maximum to the minimum value (Fig. 7). The increase in the period of oscillation as the forcing increases is thus due mainly to this slower buildup.

The system's phase–space trajectory tends, after a fairly short transient, to a closed orbit, called a limit cycle. The projection of this limit cycle onto the two phase planes of TD versus BKE and (maximum) subpolar transport $|\psi_{po}|$ versus (maximum) subtropical transport ψ_{tr} is shown in Figs. 8b and 8c, respectively, for BLR = 0.88. Figure 8a is the same as Fig. 6d but now with the time series for TD added. Maximum and minimum values of the four scalar quantities displayed in Fig. 8a are marked pairwise with different symbols: open symbols at the time of minimum and filled symbols at the time of maximum. The evolution of the transport difference TD and the subpolar transport $|\psi_{po}|$ with time is denoted in Fig. 8 by solid arrows for the rapid decay and by open arrows for the slow buildup.

The TD value approaches zero quickly (from below in Fig. 8b), and deviates from zero slowly. The double-gyre circulation becomes close to antisymmetric when TD is near zero and becomes more and more asymmetric as TD deviates from zero. During this slow part of the TD evolution, the subtropical and subpolar gyre trans-

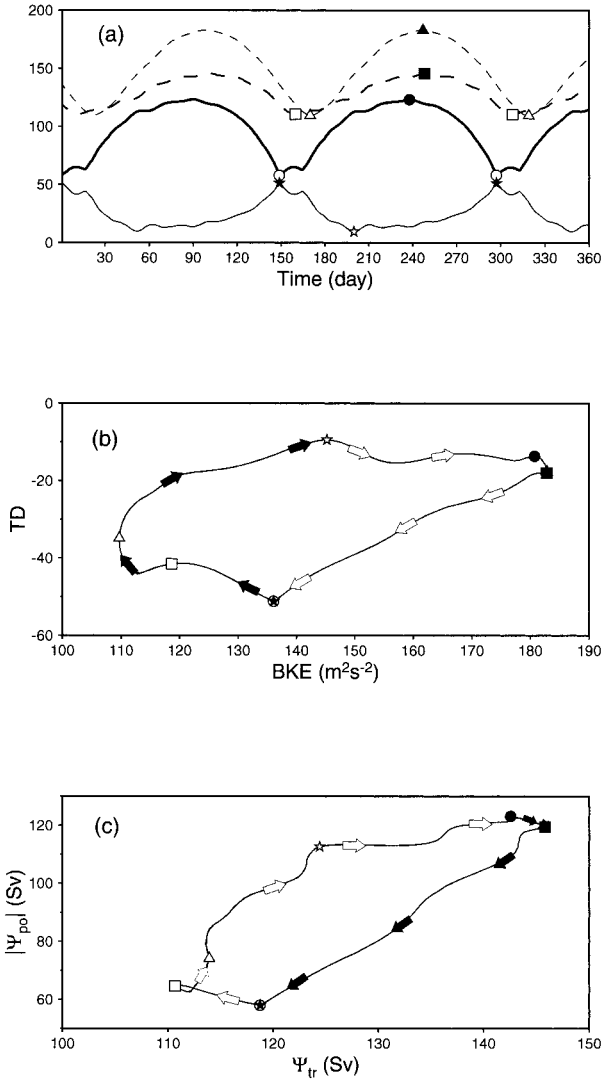

FIG. 8. Detailed evolution of a periodic solution just before transition to aperiodicity, at BLR = 0.88. (a) Time series of the subpolar gyre transport ($|\psi_{po}|$, heavy solid line), the subtropical gyre transport (ψ_{tr}, dashed line), the basin kinetic energy (0.1 × BKE, dotted line), and the transport ratio (100 × |TD|, light solid line). This panel is essentially the same as Fig. 6d, except that the curve for TD (nondimensional) has been added, and that total values, rather than anomalies, are plotted. Maximum and minimum values for each quantity are marked by filled symbols (● for $|\psi_{po}|$, ■ for ψ_{tr}, ▲ for BKE, and ⋆ for 100× |TD|) and open symbols, respectively. (b) Evolution of the trajectory projected on the phase plane defined by 100 × TD (y axis) and BKE (x axis) for one full period. The epochs at which the four scalar quantities reach their maximum and minimum values are marked by the same symbols as those used in (a). Note that the absolute values 100 × |TD| are plotted in (a) to fit into the same plot as the transport, while 100 × TD vs BKE is plotted in this panel; TD is negative for solutions on the lower branch, like the one illustrated here. Filled and open arrows denote the rapid increase in TD (⋆ → ☆ in panel a) and the slow decrease in TD (☆ → ⋆ in panel a), respectively. (c) Evolution of the trajectory over one full period, projected now on the phase plane defined by $|\psi_{po}|$ (y axis) and ψ_{tr} (x axis); same symbols as used in (a) and (b). Filled and open arrows denote the rapid decrease in $|\psi_{po}|$ (● → ○ panel a) and the slow buildup of $|\psi_{po}|$ ○ → ● in panel a, respectively; note that the ψ_{tr} axis in panel (c) is stretched with respect to the ψ_{po} axis.

ports and BKE attain their maximum values (Fig. 8b). The subpolar gyre transport, which has a larger oscillatory amplitude than that of the subtropical gyre on this lower branch, builds up slowly and decreases rapidly (Figs. 8a and 8c). A kink in the limit cycle occurs during the slow buildup, near the minimum of ψ_{tr} (Fig. 8c) and appears to contribute further to the slowdown of the buildup process as BLR increases. The kink starts to develop at BLR = 0.86 (Fig. 6c) and results in an abrupt increase in the length of time for the subpolar gyre to build up (solid line in Fig. 7) and hence in the oscillation period.

Figure 9 shows the same two projections—on the (TD–BKE) plane and ($|\psi_{po}|$–ψ_{tr}) plane—of the limit cycle as in Figs. 8b and 8c; they are plotted for the same four BLR values 0.81, 0.83, 0.86, and 0.88 as in Fig. 6, but now for both the upper and the lower branch. The plots are based on daily data for each run's final 5 yr. As BLR increases, the TD values approach zero along the periodic solution's limit cycle (see Fig. 9a). The limit cycles become more and more elongated, as seen in both projections, and the extreme values of the transport in the weaker and the stronger gyre become closer and closer to each other, that is, to the diagonal in Fig. 9b. This can also be seen directly in Figs. 1d,e (where the transports are nondimensional), as well as in Fig. 1b.

The time-dependent evolution of the streamfunction field provides some insight into the dynamics of the positive and negative feedbacks whose interplay gives rise to the periodic solutions. Figure 10 shows seven snapshots of the streamfunction field for successive phases during one full 110-day cycle of a periodic solution at BLR = 0.83; this solution belongs to the lower branch, on which the subtropical gyre is more intense. The mean of the streamfunction over the full cycle is also shown. Similar processes act on the upper branch (not shown).

Since the changes in the strength of the subpolar gyre lead those in the subtropical gyre and in BKE, the first snapshot is taken at $t = 0$, when the subpolar gyre transport is at its maximum. At $t = 17$ days, the subtropical gyre transport and BKE are at their maximum, while the subpolar and subtropical gyre transports and BKE are at their respective minima at $t = 51$, $t = 60$, and $t = 72$ days. At $t = 39$ and $t = 84$ days, the subpolar transport is at about two-thirds and one-third of its total range. The subtropical and subpolar recirculation vortices interact nonlinearly across the narrow area where the two western boundary currents merge and form a strong zonal jet.

At $t = 0$ and $t = 17$ days, the subpolar and subtropical recirculation vortices are both fully developed, in terms of both their size and magnitude, and form a nearly antisymmetric dipole, since the two transport maxima are close in time to each other. The normalized transport difference TD is closest to zero just two days before the subpolar gyre transport is at its maximum. Due to

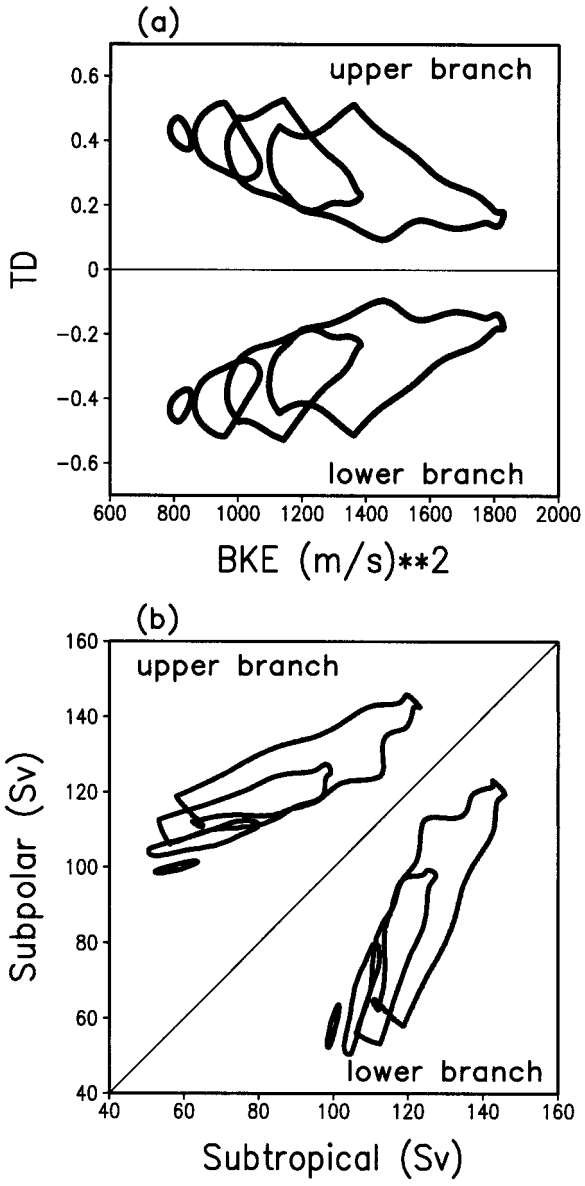

FIG. 9. Limit cycles for four periodic solutions on both branches; they correspond to the BLR values used in Figs. 6 and 7. The two projections are on the phase plane defined by (a) TD (y axis) vs BKE (x axis) and (b) $|\psi_{po}|$ (y axis) vs ψ_{tr} (x axis). As BLR increases, the trajectories become more and more elongated. The elongated end tends toward TD = 0 in panel (a) and toward the diagonal in panel (b); the largest transport value for the weaker gyre thus becomes closer to the smallest transport for the stronger gyre as the forcing increases, on both branches.

the slight asymmetry, the stronger anticyclonic vortex drags the cyclonic vortex southeastward (t = 0–60 days); this results in the generation of a weaker secondary anticyclonic vortex that detaches from the subtropical recirculation vortex (t = 51–72 days). The penetration of the subpolar recirculation vortex into the subtropical region in turn induces the northwestward intrusion of part of the subtropical water, and smaller vortices detach from the subpolar recirculation vortex in association with this northward penetration of subtropical water. The recirculation dipole shrinks during this stage, and the zonal penetration scale of the jet is reduced.

The southeastern tail of the subpolar vortex is located at its southernmost position at t = 51 days, when the subpolar transport attains its minimum value, and the meander to the east of the dipole reaches its maximum amplitude. Here TD is at its minimum 2 days before the subpolar gyre transport is at its minimum. As time goes on, the subpolar gyre recedes and intensifies, followed by the intensification of the subtropical gyre (t = 72–84 days). The smaller vortices merge back into the main vortex dipole at this time, the amplitude of the meander decreases, and the zonal penetration scale increases again. By day 110, the streamfunction pattern is exactly the same as that at t = 0.

The periodic solution thus evolves due to the vortex–gyre interactions, and the growth and decay of the meander east of the recirculation dipole. Jiang et al. (1995) and Speich et al. (1995) also noted the associated splitting of smaller vortices from the main vortex dipole, their interaction with each other, and eventual merging back into the dipole. For periodic solutions on the upper (not shown) and lower branch, the jet is straightest and most extended when the two gyres are closest in strength to each other, and the recirculation dipole is most antisymmetric. The relatively rapid phase of jet shortening, dipole tilting, and increase in downstream meandering is the relaxation phase of the oscillation. Its buildup phase corresponds to the merging of fragmented vorticity of opposite signs into the gradually stronger and more antisymmetric dipole, accompanied by an extension and straightening of the eastward jet.

The instantaneous streamfunction anomalies are shown in Figs. 11a–g; they correspond to the difference between the streamfunction fields in Figs. 10a–g and the mean streamfunction field shown in Fig. 10h and, again, in Fig. 11h. The anomalies resemble an elongated wave pattern, with curved wave fronts that are roughly perpendicular to the SW–NE direction. The strongest anomalies are localized adjacent to the first trough and crest of the large meander immediately downstream from the dipole.

To examine more closely the propagation characteristics of these, a time series of anomaly patterns along the SW–NE oriented line segment $\overline{PQ}$ in Fig. 11a is plotted in Fig. 12, together with the mean streamfunction along the line. The straight line $\overline{PQ}$ passes approximately through the cores of the successive positive and negative anomaly patches. The southwestward propagation of the anomaly field is obvious from Fig. 12a. Its phase speed is of about 10 cm s^{-1} on average; this speed is fairly nonuniform along the line segment $\overline{PQ}$ and appears to vanish toward the Sverdrup interior of the subpolar gyre, near point Q, where the amplitude of the oscillation also tends to vanish. The average speed

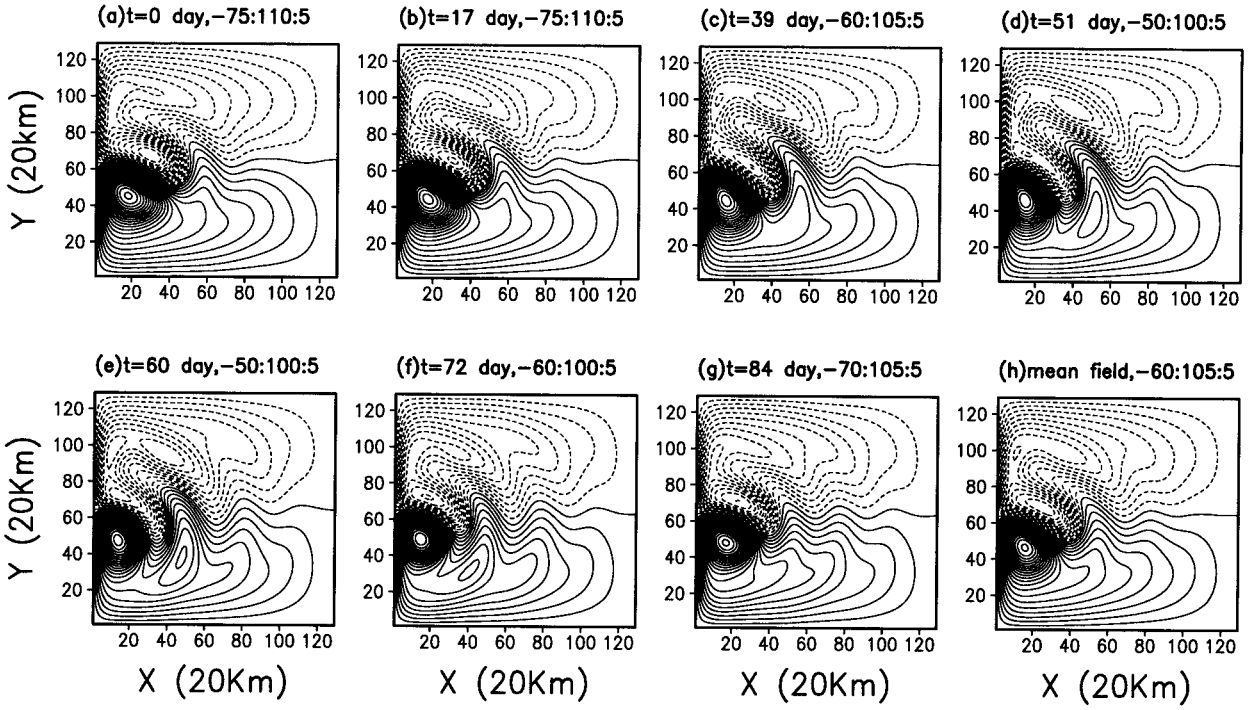

FIG. 10. (a)–(g) Snapshots of the streamfunction field during one full period (110 days) of a periodic solution on the lower branch at BLR = 0.83 and (h) the mean streamfunction for this solution. The timing of each snapshot is indicated in the legend of the corresponding panel; the reasons for the selection of these times are given in the text.

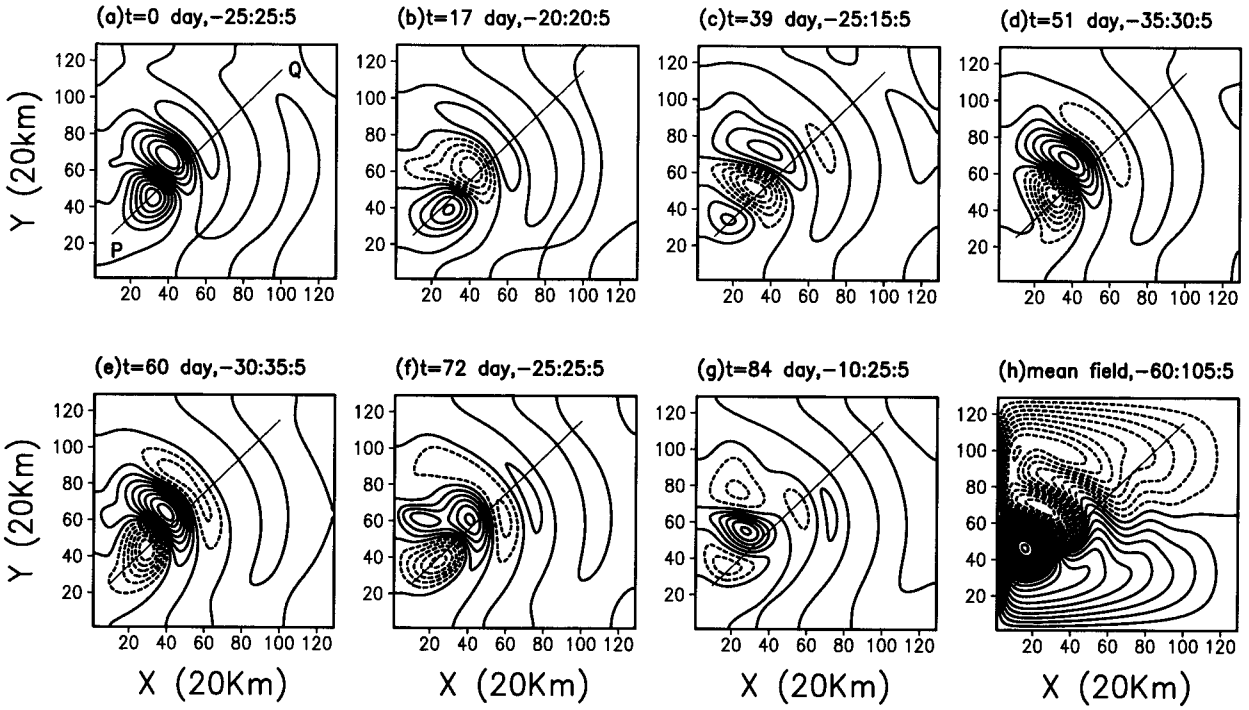

FIG. 11. (a)–(g) Streamfunction anomalies at each stage in Figs. 10a–g and (h) the mean streamfunction (same as Fig. 10h).

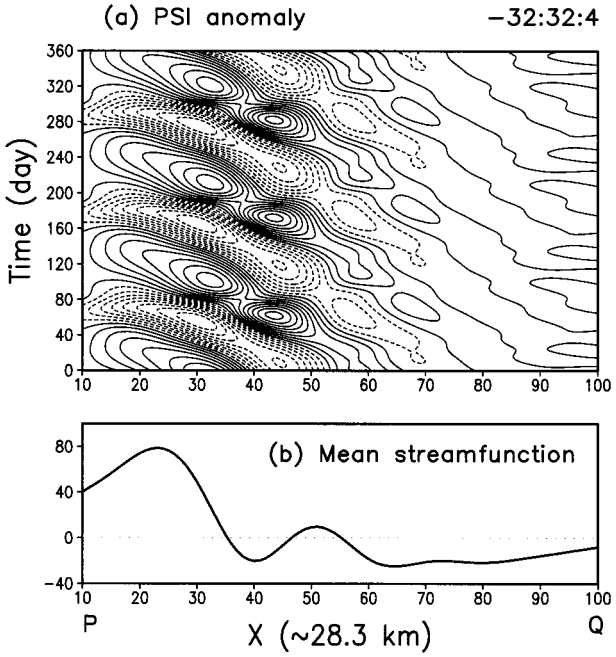

FIG. 12. NE–SW propagation of streamfunction anomalies in the periodic solution of Figs. 10 and 11. (a) Time–space plot of streamfunction anomalies along the line segment $\overline{PQ}$ in Fig. 11a for 1 yr; and (b) mean streamfunction along line. The mesh size Δl along the line $\overline{PQ}$ equals approximately 28.3 km and the distance between the two extreme points is $90\Delta l$.

of 10 cm s^{-1} is much smaller than the model's free Rossby wave speed in water at rest, which is $O(1$ m $s^{-1})$.

The period of the oscillation increases as the forcing increases, and this is mainly due to an increase in the time it takes for the recirculation vortices to attain their maximum transport (see again Figs. 6–9). The streamfunction for two periodic solutions at the time of minimum BKE is shown in Figs. 13a,b, at BLR = 0.83 and 0.88, respectively. A short zonal penetration scale, large downstream meanders, and strong eddy generation characterize this phase of the oscillation. As the forcing increases, more secondary vortices are generated and they become stronger and larger. The increase in the oscillation period seems to be associated with the fact that, as the forcing increases, it takes longer for the main recirculation vortices to absorb the detached eddies with the same sign of the vorticity, respectively, and attain therewith their maximum intensity.

2) PHYSICAL MECHANISMS

Subannual oscillation periods were also found in a QG barotropic double-gyre model driven by asymmetric wind forcing (Moro 1990). In reduced-gravity 1.5-layer models, whether shallow water or QG, periodic solutions on the upper branch have subannual periods, while those on the lower branch have interannual periods (Jiang et al. 1995; Speich et al. 1995; Dijkstra and Katsman 1997). The interannual and subannual variability has been attributed to advective processes in and near the recirculation vortex and to Rossby basin modes, respectively (Jiang et al. 1995; Dijkstra and Katsman 1997). In the present barotropic SPEM, however, periodic solutions on both branches have the same periods, amplitude, and mean energy level at a fixed BLR value.

Linear stability analysis of single-gyre solutions in a barotropic model revealed four main types of instabilities that may trigger time-dependent flows (Sheremet et al. 1997; see also Meacham and Berloff 1997a, b): (i) basin modes of Rossby waves, (ii) a wall-trapped

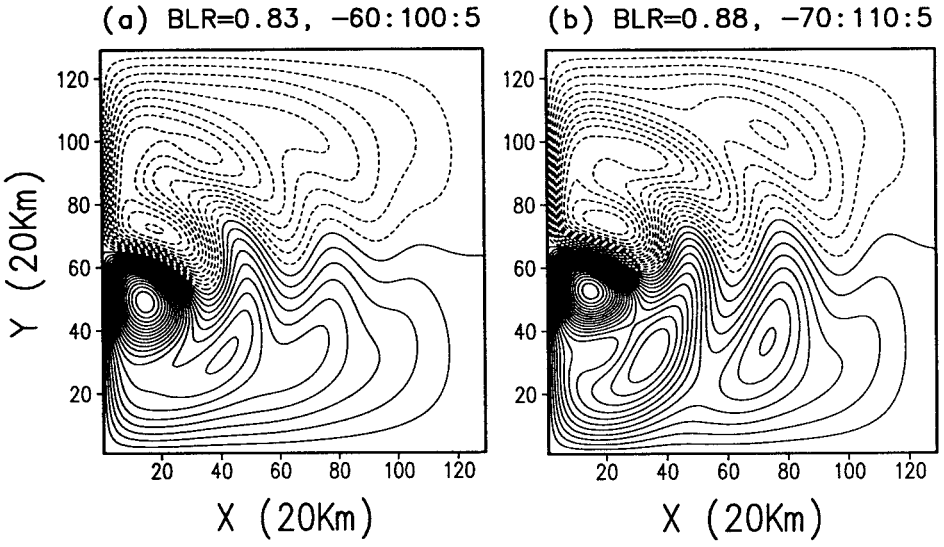

FIG. 13. Streamfunction field at the time of minimum kinetic energy for two periodic solutions on the lower branch at (a) BLR = 0.83 and (b) BLR = 0.88.

shear instability of the western boundary current, (iii) recirculation zone modes of two distinct kinds, and (iv) a resonant mode that represents a coupling of the recirculating vortex and of selected Rossby basin modes. Our model's streamfunction anomalies (see Figs. 10–12) are largest in the vicinity of the recirculation dipole and decay toward the interior of both gyres. The present oscillatory instability is thus clearly not due to an excitation of Rossby basin modes, which differ from each other by the number and shape of their nodal lines, but have all minima and maxima of comparable amplitude. It differs, furthermore, from the barotropic instability of the western boundary currents discussed by Ierley and Young (1991) and found also in QG single-gyre models by Meacham and Berloff (1997b) and other authors (see below) since this instability is characterized by eddies trapped within the western boundary current.

The instability of the western boundary current occurs first in the work of G. R. Ierley, V. M. Kamenkovich, V. A. Sheremet, and colleagues as the forcing increases. It precedes the formation of their single recirculation vortex (in the northwest corner of their subtropical gyre: see also chapter 2 of Pedlosky 1996). This instability is the first one to arise when the Reynolds number is low, and the basin aspect ratio L_y/L_x equals unity (Meacham and Berloff 1997b; Sheremet et al. 1997), in a single-gyre QG barotropic model with no-slip boundary conditions at the western and eastern walls. It does not appear, however, when the gyre aspect ratio is 0.5, like here, while it dominates in a meridionally long basin with aspect ratio 2.0 (Meacham and Berloff 1997b). The shear instability of the western boundary current is also precluded from appearing in the present model due to the use of free-slip boundary conditions (e.g., Kamenkovich et al. 1995; Sheremet et al. 1995; Berloff and McWilliams 1999b).

As shown by Ierley and Young (1991) and the authors just mentioned, this instability is wall trapped; it has therefore limited incidence on the subsequent evolution of the basinwide flow as the forcing is increased, or the lateral dissipation decreased, further. Its absence here is thus not a major concern—to the contrary, it helps diagnose the physical nature of the subannual variability that does play a major role in our model.

In the single-gyre models mentioned above, the wall-trapped instability is followed by that of a recirculation zone mode. The latter has been associated with the breakdown of the western boundary current turning smoothly into an eastward jet. In the single-gyre numerical simulations, the recirculation vortex in the subtropical gyre's northwest corner has a shape that does resemble that of Sheremet et al.'s (1997) ''recirculation gyre'' eigenmode; we prefer to distinguish throughout between our (two) recirculation *vortices* and the basinwide *gyres* (see also GFS).

The bifurcation diagram of the single-gyre models is of the S-shaped type (see Fig. 2 of Sheremet et al.'s paper) that is associated with two back-to-back saddle-node bifurcations typical of multiple equilibria (e.g., Guckenheimer and Holmes 1983; Ghil and Childress 1987, sections 6.3 and 10.2). Sheremet et al.'s ''recirculation gyre'' eigenmode, the first of their two kinds of ''recirculation zone'' instabilities, is a nonoscillatory instability. It corresponds to the first one of the two aforementioned saddle-node bifurcations [''lower nose,'' in the terminology of Sheremet et al. (1997)]. It is therefore not of immediate interest here, as our bifurcation sequence starts with a pitchfork bifurcation before reaching the supercritical Hopf bifurcation discussed in the previous subsection.

The subannual oscillation found here is due to the periodic changes in the recirculation dipole's intensity and orientation (see also GFS) and the associated interactions with the flow in the rest of the basin. A comparison of Fig. 11 here with Sheremet et al.'s (1997) Figs. 10a,c strongly suggests that our oscillation is due to an asymmetric version of their single-gyre resonant mode. The process is similar to that found on the lower branch in 1.5-layer and 2-layer, double-gyre circulation models with no-slip boundary conditions (Jiang et al. 1995, Fig. 8; Speich et al. 1995, Figs. 8a and 9; Dijkstra and Katsman 1997). The only difference is that because of the present model's mirror symmetry the period here on both branches is subannual, like on the upper branch in those models. The instability for those 1.5-layer and 2-layer models is essentially baroclinic, and manifests itself differently on the upper and lower solution branches as Rossby basin modes and resonant modes, respectively.

In those models, as well as the present one, the dipole's interaction with the periodic changes in the downstream meander's intensity and the associated shedding, mutual deformation, and subsequent merger of eddies is rich in details (e.g., Fig. 8b of Speich et al. 1995). Some of these details resemble aspects of Sheremet et al.'s (1997) second kind of recirculation zone mode (their Fig. 12). This mode seems to be synchronized here with the subannual, larger-scale behavior of resonant mode type, which is consistent with its relatively low frequency in the single-gyre models.

b. Aperiodic solutions

Starting from a periodic solution on the lower branch at BLR = 0.88, an aperiodic solution was obtained by increasing BLR to 0.90 (see Fig. 1 again). Shown in Fig. 14a is the 90-yr evolution of TD and BKE for the latter solution; the first 30 yr of the evolution are identical to those shown in Figs. 1b and 1c, respectively. Both quantities now oscillate aperiodically, as spells of a shorter, subannual period of 5–6 months (see Fig. 14b) alternate with spells of a longer interannual period of 10–25 months (see Fig. 14c). The subannual limit cycle (see Figs. 8 and 9) seems to coexist with a new, inter-

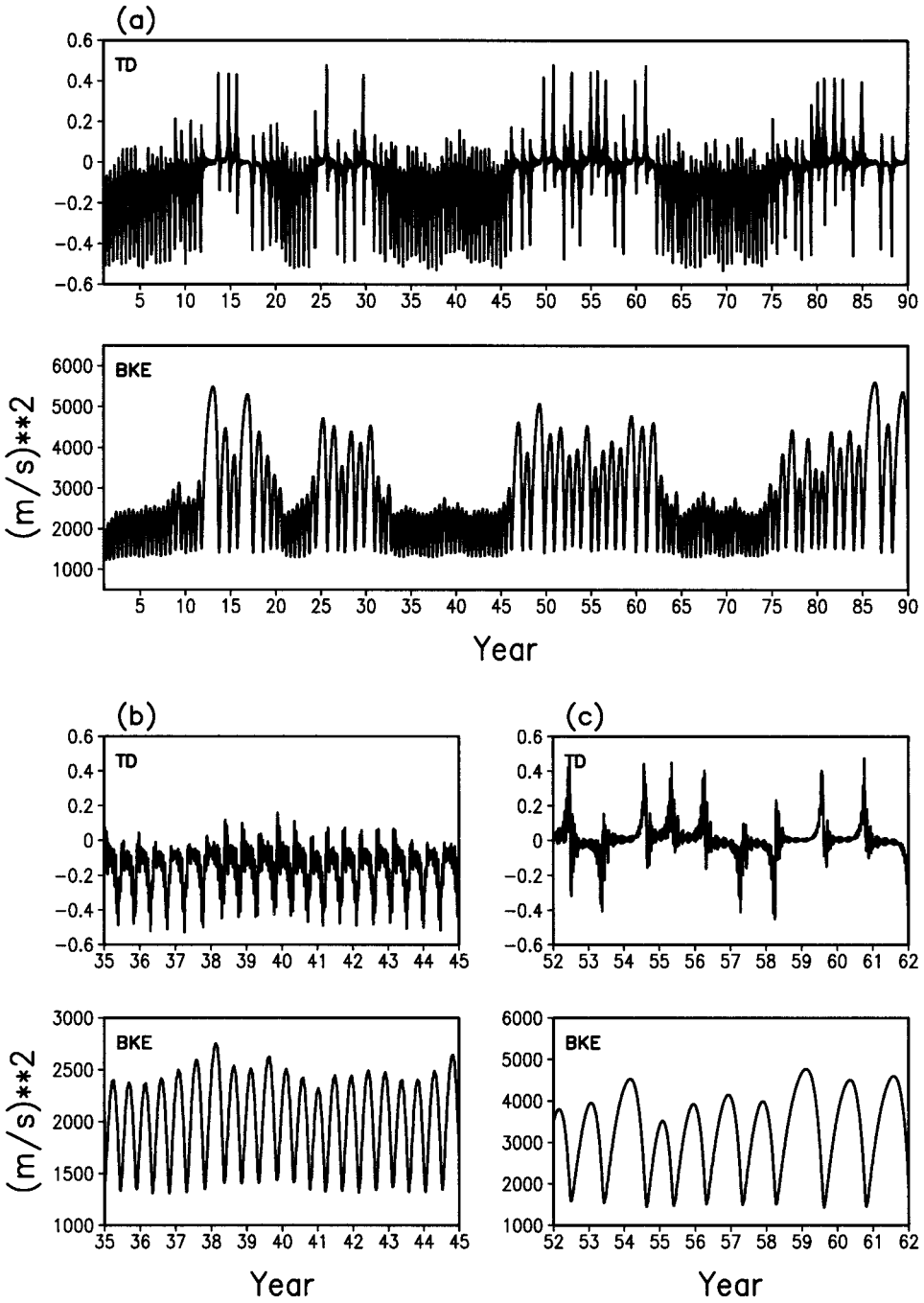

FIG. 14. Basin kinetic energy BKE and the normalized transport difference TD as a function of time for an aperiodic solution on the lower branch (a) for the entire 90 years (b) for 10 years of a short-period episode, and (c) for 10-years of a long-period episode.

annual limit cycle. The alternation between the two timescales, sub- and interannual, occurs in turn on an interdecadal scale: the two kinds of spells, sub- and interannual, last 10–15 yr each. A similar type of even lower-frequency variability also appeared during the transition to a chaotic circulation in a single-gyre model (Berloff and Meacham 1998).

The mean BKE is lower during the shorter-period episodes than during the longer-period episodes (see lower panel of Fig. 14a). Such spontaneous transitions between two types of solutions have also been found in other studies of the wind-driven circulation (McCalpin and Haidvogel 1996; Jiang and Ghil 1997). It can be seen in the upper panel of Fig. 14a that the normalized

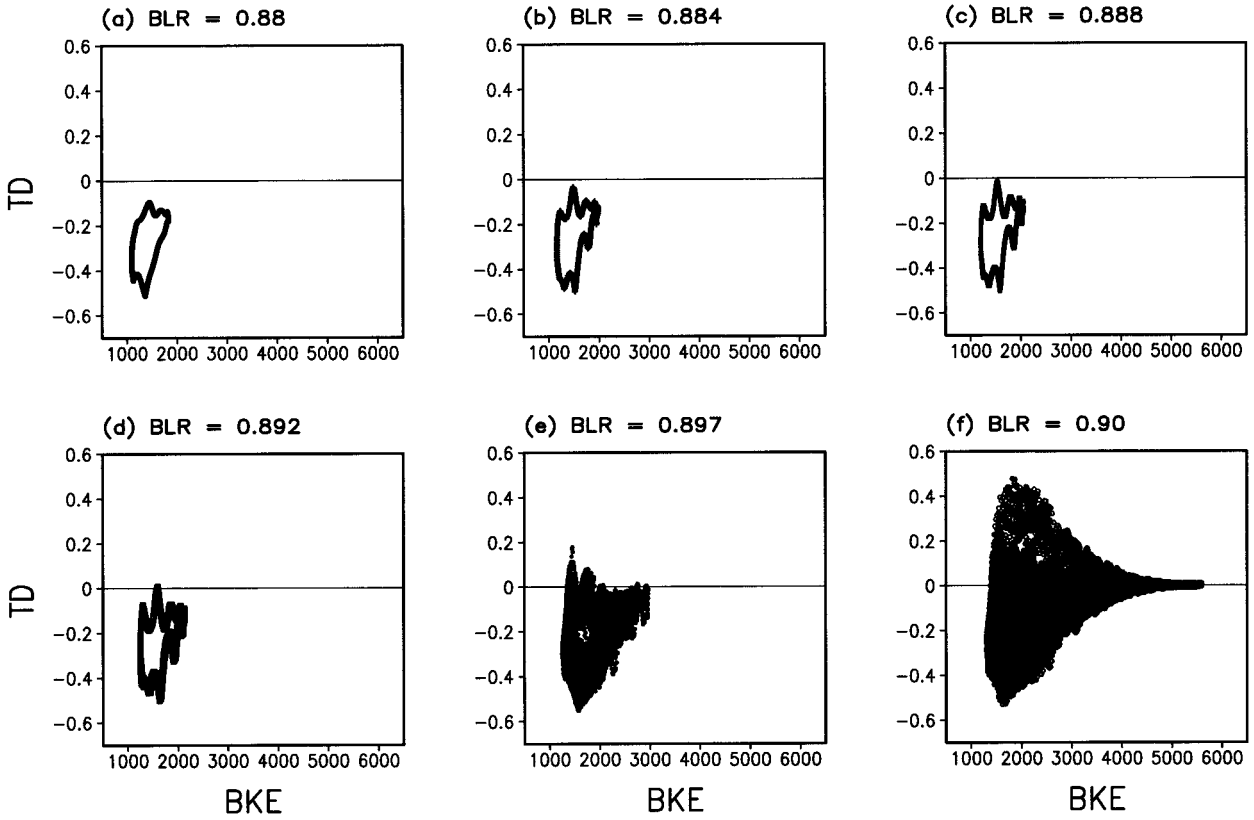

FIG. 15. Model trajectory projected on the phase plane defined by TD (y axis) and BKE (x axis) for four periodic solutions (a–d) and two aperiodic solutions (e–f) on the lower branch. The corresponding BLR values are given in the legend of each panel.

transport difference TD peaks intermittently at large positive values during the longer-period episodes, while it remains mostly negative during the shorter-period episodes. Note that the aperiodic solution in Fig. 14 was obtained from a periodic solution bifurcated off the lower branch, whose TD remains negative over the full cycle.

As the transition from a periodic solution to an aperiodic solution is rather abrupt, we further divided the BLR interval between 0.88 and 0.90 into five subintervals, each of which corresponds to an increase in the wind stress by 0.02 dyn cm^{-2}, from 2.0 dyn cm^{-2} to 2.1 dyn cm^{-2} overall. The six solutions obtained for BLR = 0.880, 0.884, 0.888, 0.892, 0.897, and 0.900 are projected onto the (TD–BKE) plane in Figs. 15a–f. The solution in Fig. 15a is the same one shown in Fig. 6d and in the lower half of Fig. 9a (the largest and rightmost limit cycle there). The solution in Fig. 15f is the same one whose time evolution is shown in Fig. 14. The projections are based on daily data after removing the first 10 yr of each run. The model was run for 20, 20, 20, 40, and 60 yr respectively, from Fig. 15a to Fig. 15e, starting from the solution obtained before with a smaller wind stress value. The maximum TD value approaches zero as the wind stress increases, and it crosses the zero line when BLR = 0.892.

Time series of the BKE for BLR = 0.888, 0.892, and 0.897 are shown in Figs. 16a–c. A careful examination of the time series at BLR = 0.892 (Fig. 16b) reveals that the peak values in the high-energy phase are slightly different, hence the solution is not exactly periodic. A slight further increase in the wind stress from BLR = 0.892 to BLR = 0.897 gives rise to a definitely aperiodic solution in Fig. 16c.

The transition to aperiodicity seems thus to be associated with the subannual limit cycle that arises by Hopf bifurcation from the lower branch touching the mirror-symmetric steady solution, which is unstable at this BLR value. The latter is characterized by TD = 0 and high BKE values, as found by numerical continuation methods in 1.5-layer shallow-water (Speich et al. 1995) and barotropic QG (Primeau 1998) models, and by quasi-Newtonian methods in a barotropic QG model (Cessi and Ierley 1995). The mirror-symmetric portion of an approximately ''figure eight'' shaped trajectory, circling both the upper and lower branch of steady solutions seems to be rapidly established as BLR increases from 0.892 through 0.897 to 0.900 (see Figs. 15d–f).

Figure 17 shows the power spectra of the ψ_{tr} time series for BLR = 0.88, 0.888, and 0.897. The spectra were calculated using version 3.1 (see http://www.atmos.ucla.edu/tcd) of the Dettinger et al. (1995) Sin-

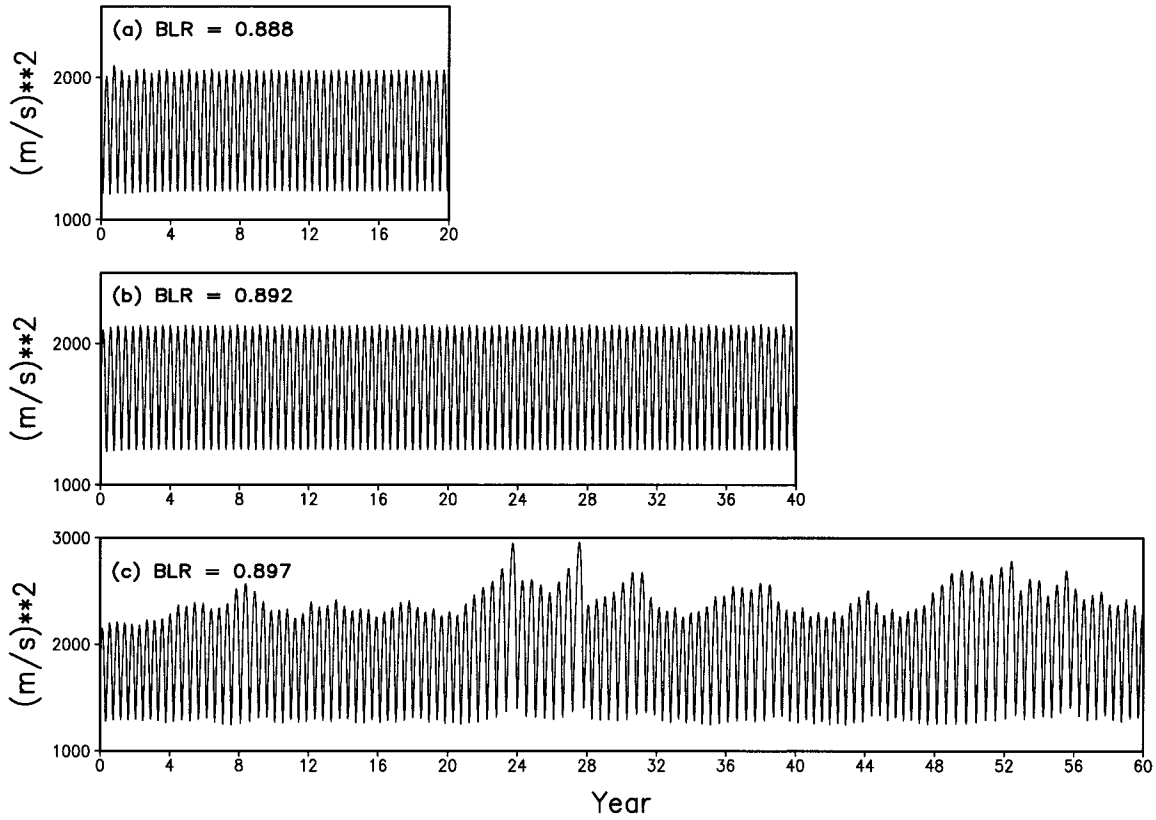

FIG. 16. Basin kinetic energy BKE as a function of time for three solutions at (a) BLR = 0.888, (b) BLR = 0.892, and (c) BLR = 0.897.

gular-Spectrum Analysis Toolkit. The dominant periods of oscillation at the three BLR values are all subannual and they increase from 148 days ≈ 5 months in Fig. 17a to 182 days ≈ 6 months in Fig. 17c as the forcing increases. The only other peak for BLR = 0.88 is the first harmonic of the dominant subannual period of 148 days, whose period equals 74 days (Fig. 17a). A distinct peak emerges, at 19 days, for BLR = 0.888. This peak persists, with exactly the same period, at BLR = 0.897. Plots of both ψ_{tr} and ψ_{po} for BLR values greater than 0.88 all exhibit a small amplitude oscillation of 19-day period superimposed on the main, subannual-scale oscillation (not shown).

The peak at 19 days thus behaves differently from the subannual one in its parameter dependence: The period of the former stays fixed as BLR increases, while that of the latter increases. The two oscillatory modes are probably due, therefore, to two distinct physical mechanisms. As we shall see, the mechanism of the 19-day oscillation appears to be closely related to a Rossby basin mode.

Sheremet et al. (1997) have shown, in their single-gyre model, that the frequency of the model's forced, viscous basin modes is very close to that of free, linear Rossby basin modes. Moreover, the spatial patterns of the former are just linear combination of the degenerate pairs of eigenvectors of the latter. The dispersion relation of our basin's free Rossby modes is given by

$$\sigma = 0.5\beta[(l\pi/L_x)^2 + (m\pi/L_y)^2]^{-1/2}, \qquad (9)$$

where l and m denote the horizontal mode numbers in the zonal and meridional direction, respectively. With $l = 2$, $m = 1$, and $L_x = L_y = 2560$ km, the period of the corresponding free basin mode is 20 days, which is very close to the 19-day peak. This coincidence is supported further by the 19-day mode's spatiotemporal pattern, whose study we take up in section 5b.

For the aperiodic solution at BLR = 0.897 (Fig. 17c), the dominant subannual peak, as well as the smaller peak at 19 days, are broader than those in the spectra for periodic or nearly periodic solutions at BLR = 0.888 and 0.892 (Figs. 17a,b). At the same time, the continuous spectral background at low frequencies has increased more than 100 times above the level recorded in the two preceding panels.

The spectral content of the transport time series increases at lower frequencies by another two orders of magnitude for BLR = 0.90 (Fig. 18a). Only a spectral peak with a near-annual period (384 days) is obtained (Fig. 18a) for all 90 years of data. Spectral analysis of the ψ_{tr} time series during a high-energy episode (from year 46 to year 63 in Fig. 14) and a low-energy episode

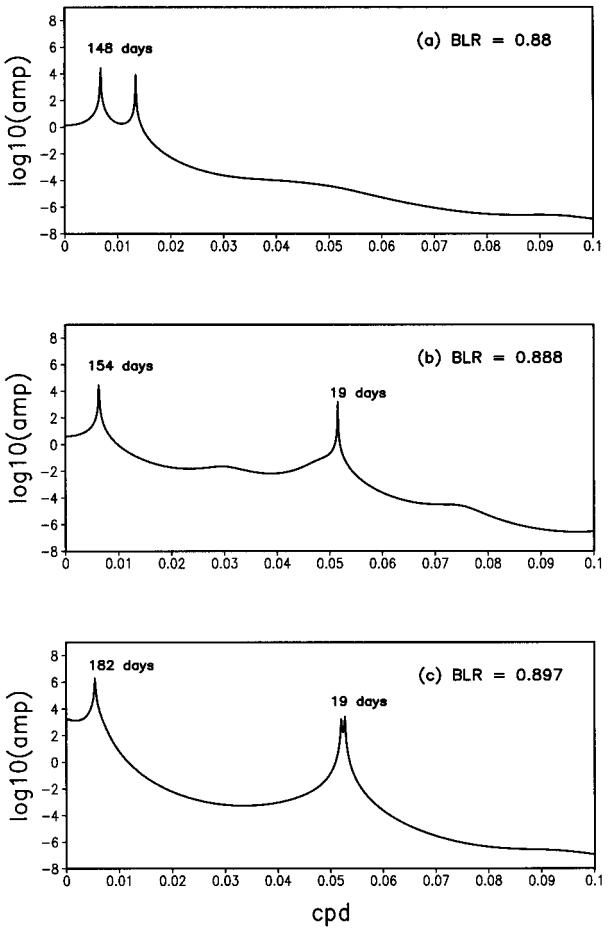

FIG. 17. Maximum-entropy spectra of the ψ_{tr} time series at (a) BLR = 0.88, (b) BLR = 0.888, and (c) BLR = 0.897. The spectra are calculated based on daily values after removing 10 yr of the initial transient stage. The series were prefiltered by projection onto the leading principal components of each series' singular-spectrum analysis. The prefiltering used the four leading principal components in (a) and (b), and eight components in (c). The order of the method (number of lags) is 50. The dominant periods of oscillations are marked.

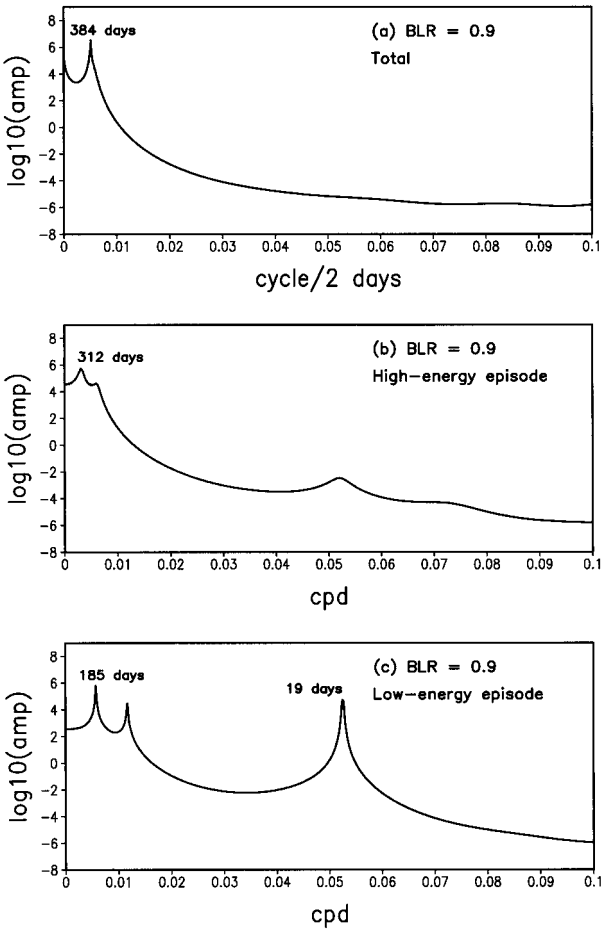

FIG. 18. Maximum-entropy spectra of the ψ_{tr} time series of the aperiodic solution in Fig. 14 for (a) all 90 of data, (b) data during the high-energy episode that lasts from year 46 to 63, and (c) data during the low-energy episode from year 33 to 45. The spectra are calculated based on data sampled every two days after removing the initial 10 years for (a), and based on daily data for (b) and (c). The order of the method is 50, and the prefiltering used the eight leading principal components.

(from year 33 to year 45 in Fig. 14), however, separates a near-annual (Fig. 18b) from the subannual (Fig. 18c) peak and enhances each peak separately. The 19-day peak is much sharper in the low-energy than in the high-energy episode due to the small amplitude of the Rossby basin mode.

Instantaneous snapshots of the streamfunction field evolution for BLR = 0.90 are shown in Fig. 19 at six selected days during the longer-period episode between day 21 728 (~year 60.35 in Fig. 14a) and day 22 340 (~year 62.05 in Fig. 14a). The six snapshots correspond to the high- (Figs. 19a and 19d) and low-energy (Figs. 19c and 19f) states, and positive TD (Fig. 19b) and negative TD (Fig. 19e) states that occur during this episode; the extreme-energy phases all involve very low values of |TD|. The evolution of the streamfunction field during the short-period episodes (not shown) is similar to that of the purely periodic solutions illustrated in Fig. 10.

The high-energy states of Figs. 19a and 19d are characterized by a strong and nearly antisymmetric recirculation dipole, long penetration scale of the zonal jet, weak downstream meandering, and no eddy generation. The states with the highest asymmetry, whether having positive (Fig. 19b) or negative (Fig. 19e) TD values, are characterized by a short penetration scale, strong meandering, and substantial eddy generation. These states occur between the previously mentioned high-energy states of either TD sign and the corresponding low-energy states (Figs. 19c and 19f) that have the same sign but a low value of TD. Both extreme-TD states, the positive and negative sign ones, are nearly mirror-symmetric with respect to each other, and so are the high- and low-energy states. Essentially the whole evo-

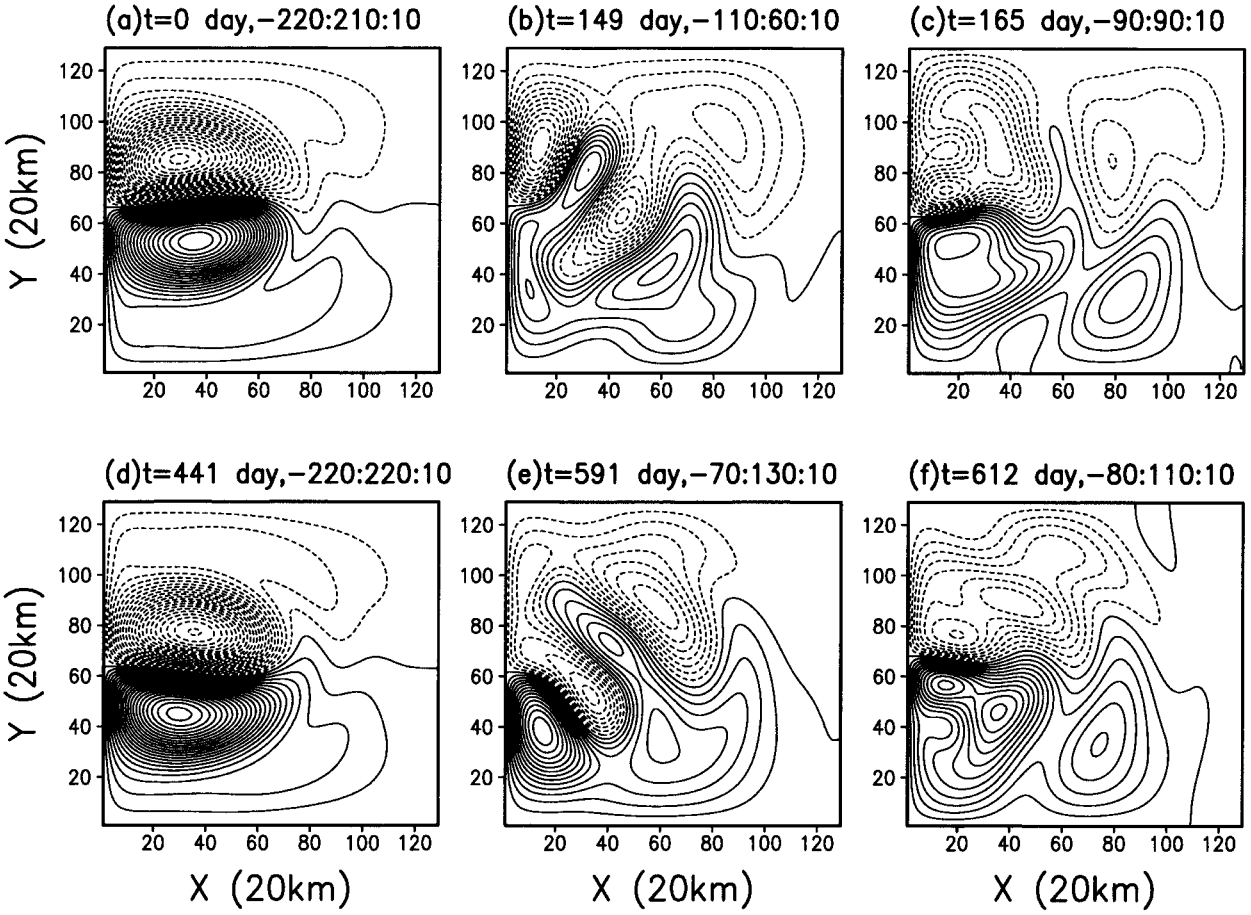

FIG. 19. Streamfunction field snapshots taken during a long-period episode that lasts for 612 days: (a) and (d) high-energy states; (c) and (f) low-energy states; (b) positive TD and (e) negative TD states. The episode illustrated here occurred between year 60.35 (day 21 728) and year 62.05 (day 22 340) in Fig. 14.

lution from day 441 to day 612 mirrors the evolution from day 0 to day 165.

The solution trajectory can visit a number of times in succession high- and low-energy states with the same sign of TD, each time visiting a high-|TD| state of the same sign in between. The transition from a high-TD state of one sign to that of another sign always occurs through a high-energy state with near-zero TD. The aperiodic solution's sequence of phases is entirely consistent with the hypothetical presence nearby in phase–parameter space of a ''figure eight,'' mirror-symmetric homoclinic orbit. This orbit occurs for a BLR value between 0.897 and 0.900, and passes through the unstable mirror-symmetric steady solution.

It appears that the unstable antisymmetric steady solution, along with the likewise unstable asymmetric steady solutions and the subannual-scale periodic solutions are all imprinted on the aperiodic solution. It is the interaction of these solutions belonging to the different branches that probably causes the interannual and interdecadal variability of the system.

5. Concluding remarks

a. Summary

We have studied successive bifurcations in a barotropic model of the double-gyre ocean circulation. The model flow is driven by meridionally symmetric and steady zonal wind stress in a rectangular basin and dissipated by lateral friction as the Rossby number R is being varied, while keeping the horizontal Ekman number E_L fixed (see Fig. 1). The bifurcation parameter chosen is the ratio BLR $= \delta_I/\delta_M$ between the inertial and viscous boundary layer widths δ_I and δ_M. This ratio increases with the forcing and decreases with the lateral dissipation [see Eqs. (5,6)].

Our main results concern the generation of the free, internal variability in such a highly idealized model of the midlatitude ocean. This variability arises in phase–parameter space by both local Hopf bifurcation and global, homoclinic bifurcation; it encompasses subannual as well as interannual and interdecadal timescales.

The nonlinear character of the flow can be measured

by the ratio NR between the maximum transport in the stronger one of the two gyres and the linearly forced Sverdrup transport [see Eqs. (8a,b)]. As long as this ratio is close to unity (NR $\leq$ 1.58), an antisymmetric, counterrotating double-gyre circulation characterizes the flow field. The transport of both the subtropical and subpolar subgyres increase at the same rate as the forcing increases. The western boundary currents of the two gyres merge, after their separation from the boundary, to form an eastward jet. This jet becomes stronger as the forcing increases, but keeps running along the midbasin's symmetry axis (see Figs. 2a,b).

Multiple equilibria that break the model's mirror symmetry arise at moderate values of the Rossby number through a pitchfork bifurcation (at BLR = 0.635). The asymmetric solutions come in pairs, with either solution in a pair being the mirror-symmetric image of the other. In each such solution, the eastward jet meanders off the symmetry axis and takes the form of a spatially damped stationary wave (see Fig. 3). Within this moderately nonlinear multiple-equilibria regime (1.74 $\leq$ NR $\leq$ 1.86), a strong recirculation vortex forms within each gyre; the two counterrotating vortices constitute a dipole close to the domain's western boundary (see Figs. 2c,d). The stronger of the two recirculating vortices pulls the weaker one to become more and more elongated around the stronger one as the forcing increases. This results in an amplification of the eastward jet's meander immediately downstream of the dipole. The transport of the more intense gyre increases as the forcing increases, while the transport of the weaker one remains nearly the same. Hence the normalized transport difference TD between the two gyres—which is zero for the mirror-symmetric solution branch at low forcing—becomes nonzero, with opposite signs for the two stable branches of the pitchfork bifurcation (see Figs. 1b and 4).

As the forcing is further increased, each of the two steady solution branches undergoes a supercritical Hopf bifurcation, at BLR $\approx$ 0.80 (see Fig. 4). These two bifurcations give rise to mirror-symmetric branches of oscillatory solutions (see Fig. 5). The subannual periods of these solutions increase as the forcing increases from about 3.5 to about 5 months (see Fig. 6), and the character of the oscillations becomes more and more nonlinear (1.90 $\leq$ NR $\leq$ 2.21). The oscillation's nonlinearity is of the relaxation type: The length of time for the stronger gyre to ''wind up'' increases considerably faster with the forcing than the time for the ''wind down'' or relaxation phase (see Fig. 7).

The relaxation phase is also characterized by relatively rapid shortening of the eastward jet; the axis through the two centers of the recirculation dipole tilts away from the N–S direction, the amplitude of downstream meandering increases, and so does the associated secondary-eddy generation. By contrast, the slow buildup in intensity of the stronger gyre and recirculation vortex within it is characterized by the merging of the secondary eddies into the gradually stronger and more nearly mirror-symmetric main vorticity concentrations of the dipole. This, in turn, leads to a straightening and greater eastward extension of the jet (see Fig. 10). As the forcing increases, the strength and size of the secondary eddies increases, too; consequently, the process of absorbing these into the two main recirculating vortices of opposite vorticity increases and results in an increase in the oscillation period.

At the next step in ''climbing'' the successive-bifurcation ''tree,'' aperiodic flows arise (in the range 0.88 $<$ BLR $<$ 0.90; see again Figs. 1 and 15). These flows display a number of additional features, besides the subannual periodicity just described. A new period, of 19 days, appears—through a secondary Hopf bifurcation—and is quite stable as the forcing increases further, while the subannual period increases even more, from about 5 to about 6 months (see Fig. 17). To identify the nature and location of the secondary Hopf bifurcation we plotted ψ_{tr} as a function of time for the final 5-yr each of the runs at BLR = 0.88, 0.884, 0.888, and 0.897 (not shown). The 19-day oscillations become visible at BLR = 0.884 and are successively stronger at BLR = 0.888 and 0.897. The secondary Hopf bifurcation is thus also supercritical and located roughly at BLR = 0.884, but does not seem to play a major role in giving rise to the aperiodic behavior.

The transition to aperiodicity involves the increase in size and elongation of the subannual limit cycle (see Figs. 9 and 15) until the transport difference TD vanishes at one extreme of the cycle. This corresponds apparently in the model's phase–parameter space to transition through a *homoclinic*, structurally unstable orbit that connects the two mirror-symmetric limit cycles—each of which arises from and circles around one of the two previously stable steady-solution branches of the pitchfork bifurcation. These two coexisting limit cycles thus touch each other via the unstable, self-symmetric steady branch characterized by TD = 0.

In the flow field physical space, this transition corresponds to solutions that alternate between a stronger subpolar and a stronger subtropical gyre, via phases during which the two gyres are nearly equal in strength and the recirculation dipole is nearly mirror-symmetric. The latter phases are attained because the oscillation amplitude of the weaker gyre is larger than that of the gyre that is, on average, stronger. This amplitude becomes even larger as the forcing increases, and so does the average strength, which has the opposite sign, of the stronger gyre. Eventually the two oscillations' opposite phases—of algebraically highest and lowest TD—become nearly identical and permit the flow transition from one sign of TD to the other.

The fully aperiodic flow exhibits two new types of low-frequency variability, on the interannual and interdecadal scale, in addition to the subannual oscillations that lose their exactly periodic character. The interannual oscillations have a period of about 1–2 yr and are more energetic than the subannual ones with their now broad-

ened peak of 5–6 months. The aperiodic solutions are characterized by an irregular alternation between the high-energy episodes with an interannual scale of variability and the low-energy episodes dominated by subannual variability; the latter are accompanied by a stronger, but still fairly small amplitude 19-day oscillation (see Fig. 14). The associated values of NR are about 2.8 for the low-energy episodes and about 3.7 for the high-energy episodes (not shown).

The irregular transitions between the two types of episodes introduce an even lower-frequency variability, with a characteristic timescale of 10–15 yr. As a result, the low-frequency spectral power is substantially increased in the aperiodic solutions, though the subannual peak is still recognizable (see Figs. 17 and 18). During the interannual-scale oscillations, the trajectory starting near one branch visits the neighborhood of the other branch irregularly, thus generating an approximately heteroclinic orbit that ''shadows'' the homoclinic orbit through which the periodicity was lost.

b. Discussion

The highly idealized model of the wind-driven, double-gyre circulation we studied herein has produced a rich array of spatiotemporal variability, as summarized in the previous subsection. The interpretation of this variability in terms of earlier model results, on the one hand, and of the existing oceanographic observations, on the other, in the object of the present subsection.

1) MODES OF TEMPORAL VARIABILITY

In the order of increasing timescale, we have found 19-day variability, subannual variability at 3.5–6 months, interannual variability at 10–25 months, and interdecadal variability at 10–15 years. The period of the subannual variability increases as the forcing increases, and so does the width of the associated spectral peak. The interannual and the interdecadal variability arise as broadband features in the first place, rather than as sharp peaks.

Of these four modes of variability, the one that is most important in our model and best understood is the subannual mode. It arises by supercritical Hopf bifurcation (see also Jiang et al. 1995; Dijkstra and Katsman 1997) from either one of the mirror-symmetric steady solution branches. The physical mechanism of this bifurcation is a double-gyre, asymmetric version of the resonance between a Rossby basin mode and the recirculation dipole found by Sheremet et al. (1997) in a single-gyre barotropic model. This resonant mode seems to be synchronized in our model with a recirculation zone mode. The common period of these two modes is longer than that of either Rossby basin modes or wall-trapped modes. The sharp and stable peak at 19 days is apparently due to a Rossby basin mode.

Our physical explanation of the subannual mode is supported by the spatial pattern of the instability in the present model (Figs. 10–12), as well as in the reduced-gravity, shallow-water model of Jiang et al. (1995) and Speich et al. (1995). The explanation of the high-frequency peak is supported by the calculated period of a specific large-scale basin mode, 20 days versus 19 days [see Eq. (9)].

To examine more closely these identifications, we carried out an empirical orthogonal function (EOF) analysis of the streamfunction field at BLR = 0.88 (Fig. 20) and BLR = 0.888 (Fig. 21). The data for the EOF analysis at both BLR values are the respective streamfunction fields—taken to repeat the subannual oscillation four times—while the sampling interval is 2 days, to resolve the 19-day oscillation. The two leading principal components at both BLR values (not shown) are clearly dominated by the corresponding subannual period of roughly 5 months (see Figs. 17a,b). The 19-day mode is absent from the six leading principal components at BLR = 0.88, while it dominates principal components 3 and 4 at BLR = 0.888.

The spatial patterns of the leading two EOFs at BLR = 0.88 appear in Figs. 20a,b. They agree rather well with the main features of Figs. 10–12 here and the corresponding figures in the Jiang et al. and Speich et al. papers. These features are most pronounced near the recirculation vortices and decay away from them in a circular wave front pattern, as suggested by Fig. 10 of Sheremet et al. (1997). The first two EOFs are thus the two in-quadrature phases of the resonant mode, and are responsible for the dominant subannual variability.

EOFs 3 and 4 at BLR = 0.888 capture the spatial features of the 19-day oscillation and are shown in Figs. 21a,b. They account for 21% of the total variance at this BLR value, while EOFs 1 and 2 account for 45%. At BLR = 0.88, EOFs 1 and 2 (shown in Fig. 20) account for 62% of the variance, while the 19-day oscillation is absent (see above). We do not show EOFs 1 and 2 at BLR = 0.888, since they are visually almost indistinguishable from the ones at BLR = 0.88.

Like EOFs 1 and 2 in Fig. 20, EOFs 3 and 4 in Fig. 21 represent two phases of a basinwide oscillation. This oscillation differs from a Rossby basin mode in water at rest by a moderate distortion near the recirculation dipole. Otherwise its zonal and meridional wavenumbers agree overall with the values $l = 2$, $m = 1$ used in Eq. (9) to compute its 20-day period. The agreement in period and pattern is as good as the moderate spatial distortion would allow one to expect.

The interannual and interdecadal variability in our model arises from purely nonlinear mechanisms that involve interactions between the simpler oscillatory mechanisms, on the one hand, and between the model's heretofore distinct solution branches, on the other hand. This greater complexity of the solution's behavior in the time domain also entails greater spatial complexity of the solutions. The latter is consistent with the greater spatiotemporal complexity of multilayer model solu-

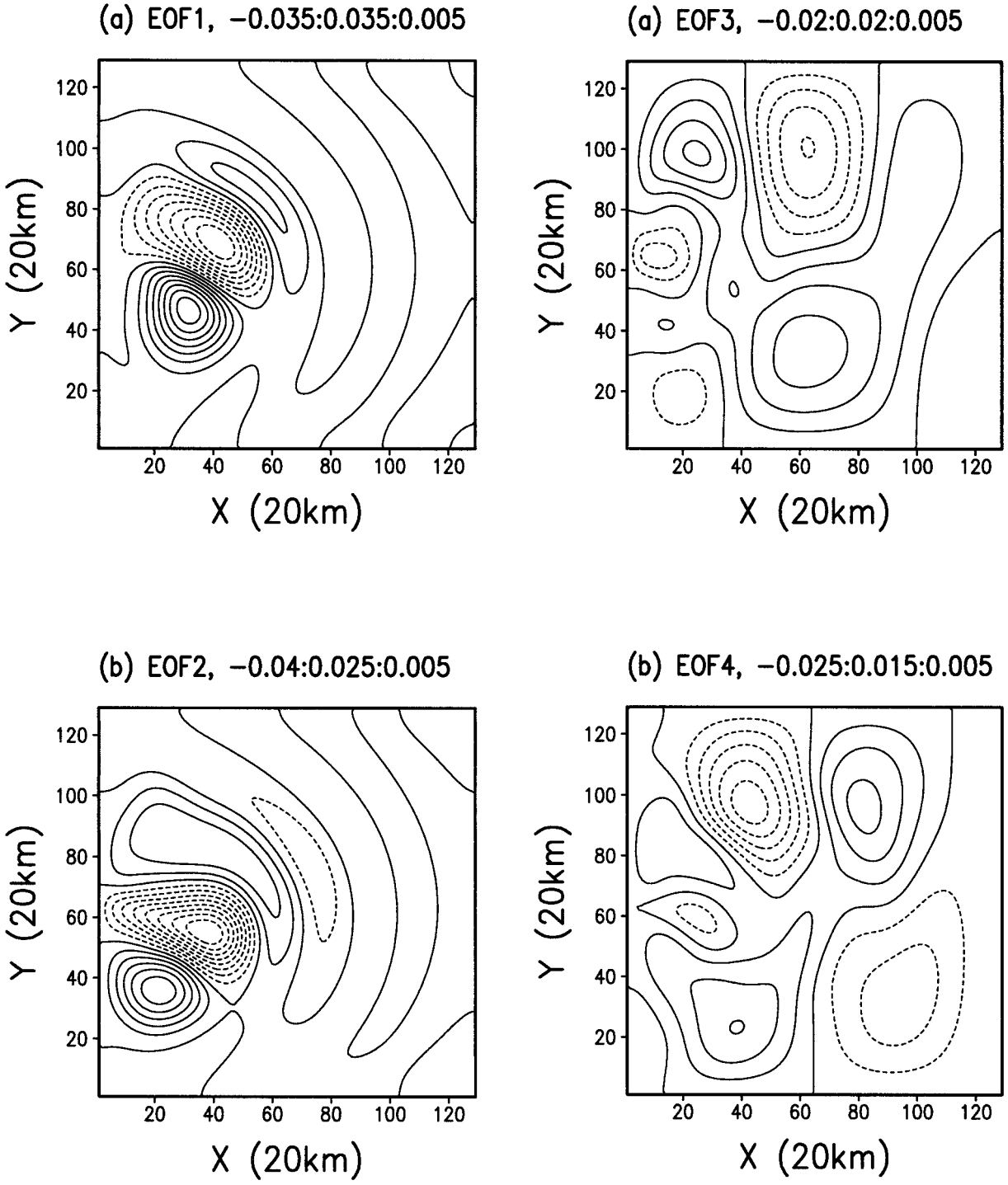

FIG. 20. The two leading EOFs of the streamfunction field at BLR = 0.88. (a) and (b) Two phases in quadrature of the subannual oscillation that dominates the variability at this value of the forcing. The spatial pattern suggests that the oscillation's physical mechanism is a resonance between the model's recirculation dipole and a Rossby basin mode.

FIG. 21. EOFs 3 and 4 of the streamfunction field at BLR = 0.888. (a) and (b) Two phases in quadrature of the 19-day oscillation that accounts for about 20% of the variance at this value of the forcing. The spatial pattern suggests that the oscillation's physical mechanism is a Rossby basin mode distorted by the presence of the recirculation dipole.

tions at higher Reynolds numbers, as described by Berloff and McWilliams (1999a).

2) Model realism

The wind-driven circulation of the major ocean basins contains typically a subtropical gyre that greatly exceeds in size and strength the subpolar gyre. This situation has inspired recent work on two types of idealized models. Single-gyre models study the subtropical gyre only (Ierley and Sheremet 1995; Meacham and Berloff 1997a, b; Sheremet et al. 1997), while double-gyre models study a subtropical and a subpolar gyre of equal or nearly equal strength (Cessi and Ierley 1995; Jiang et al. 1995; Speich et al. 1995). Both of these lines of work have used so far mostly rectangular basins and the correspondingly idealized wind stress profiles. Their results are thus both likely to provide physical mechanisms that will help explain the real asymmetric situation. In a sense, the two types of models bracket the ocean basins' real circulation.

From this perspective, it is important that our model subannual variability arises from the same kind of resonance between its recirculation dipole and a Rossby basin mode as in the single-gyre models (Sheremet et al. 1997). The subtropical recirculation vortex is a common feature of both types of models, as well as of the observations and GCM simulations. So is the major meander downstream of this vortex. The eastward jet and its meandering, however, are not restricted in the present model by the basin's northern boundary. Their variability, therefore, is expected to be somewhat more realistic than in the single-gyre models, where it is thus restricted.

Although the wind forcing used in the present study is symmetric, an antisymmetric circulation with two equal-strength gyres is only maintained for BLR ≤ 0.62. For larger BLR values the stable solutions, whether steady or periodic, are asymmetric and characterized by a spatially damped wave downstream of the recirculation vortices. Observations in the confluence zone of two western boundary currents confirm the existence of such a nearly stationary wave east of the separation of the currents from the boundary, in both the North (Chao et al. 1996; Lee and Cornillon 1996) and South (Olson et al. 1988) Atlantic. The stationary wave's amplitude decreases downstream of the recirculation dipole in our purely barotropic, flat-bottomed model. In the real ocean, however, bottom topography can increase the amplitude downstream (e.g., Mizuno and White 1983) and so can the change in character of the flow, from predominantly baroclinic near the coast to predominantly barotropic in midocean.

The subannual oscillation found in the present idealized model has a period of 3.5–6 months, which increases with the forcing. It arises at a value of the nonlinear transport ratio NR $= 1.90$, and persists into the aperiodic flow regime during its low-energy episodes, when NR ≈ 2.80. The latter value of NR agrees roughly with the observational finding of the Gulf Stream transport exceeding the basin Sverdrup transport by a factor of about 3 (Halkin and Rossby 1985; Hall 1986). Lee and Cornillon (1996) and Ide et al. (1997, unpublished manuscript) found subannual periods in the meandering of the Gulf Stream. Lee et al. (2000, manuscript submitted to *J. Phys. Oceanogr.*) and J. Brook (1998, personal communication) also found 3-month periods in two different sections of the Kuroshio.

The largest value of BLR $= \delta_I/\delta_M$ explored in this study is 0.9, at which our model's double-gyre circulation becomes aperiodic. In the real ocean, the inertial boundary layer width δ_I is as large as or larger than δ_M, the frictional (or Munk) layer width. Hence, our model results are consistent with the real ocean circulation being aperiodic in time and fairly complex in its spatial structure. The models studied heretofore have exhibited further spatiotemporal complexity as the number of layers (Dijkstra and Katsman 1997) or vertical modes (GFS) was increased, the horizontal resolution decreased (Berloff and McWilliams 1999a; GFS), and the Reynolds number increased (Berloff and McWilliams 1999a). Each one of these changes in the direction of greater realism permits additional instabilities to arise and interact with those captured by our model. The interactions between these instabilities and the degree of nonlinearity increase, in particular, when using lower values of lateral eddy viscosity, that is, higher Reynolds numbers (Berloff and McWilliams 1999a).

The main objective of the present study was, however, to examine how the crucial feature of aperiodicity emerges from a nearly linear, steady, double-gyre circulation. The mechanism of transition to aperiodicity described herein depends in an essential way on the presence of two counterrotating gyres and is thus quite different from the mechanisms described in considerable detail in the single-gyrew work of Berloff and Meacham (1997, 1998). Ours might thus be more relevant to large ocean basins in either hemisphere, while theirs could be relevant to smaller enclosed basins, like the Black Sea.

We are thus left with two questions. First, what determines, in fact, the asymmetric coexistence of a stronger subtropical with a weaker subpolar gyre in the oceans? Second, which ones of the physical mechanisms found in single- and double-gyre models are most relevant to the variability of the actual wind-driven circulation? Clearly, realistic bathymetry and wind stress profiles play a major role in answering these two questions. A number of recent simulations have used model and forcing configurations that are intermediate between those of a full GCM and the highly idealized, rectangular-domain models so far (Simonnet 1998; Dijkstra and Molemaker 1999).

In the previously mentioned companion paper by the present authors (in preparation, see section 2a), we explore a still idealized double-gyre model with asym-

metric geometry. A small rectangular bight of smaller depth, set into the western boundary of the flat-bottomed open ocean, is meant to model the effect of the East China Sea on the evolution of the Kuroshio. The suction of this bight causes an earlier detachment of the northward boundary current past it, and thus perturbs the pitchfork bifurcation of the steady states in the present version of the model (Fig. 4 here). This is but one of the future studies required to check whether the transition to aperiodic variability found in the present study is robust to boundary conditions, domain, and forcing configuration, and the vertical stratification of the ocean.

In our double-gyre, mirror-symmetric model, the periodic and steady solutions on different branches, including unstable ones, collide and interact. This gives rise to new low-frequency, highly energetic, interannual variability. Interannual periods in sea surface temperature have been observed in both the North Atlantic and North Pacific (Speich et al. 1995; Moron et al. 1998). In our model, the irregular alternation of the subannual and the interannual variability results in a major increase of broadband spectral power at interdecadal and lower frequencies.

Earlier explanations of interannual and interdecadal variability in the North Atlantic and North Pacific have emphasized coupled ocean–atmosphere modes. These modes in turn have involved either the ocean's wind-driven (Latif and Barnett 1994; Robertson 1996) or its thermohaline (Delworth et al. 1993; Chen and Ghil 1996) circulation. We do not mean to imply that these coupled modes have no relevance to a satisfactory explanation of the observed variability. The present results—along with those of earlier work cited at length in section 1 and going back to that of Veronis (1963, 1966)—merely suggest that intrinsic variability of the midlatitude ocean wind-driven circulation should be given full consideration in finding such an explanation.

Acknowledgments. It is a pleasure to thank numerous colleagues for informing us of their work in advance of publication and for useful comments. In the editorial process, the paper has benefited from the comments of Chad Coulliette and an anonymous reviewer. F. Fleuriau helped with the communications between the four coauthors, distributed at times over three continents. This work was supported by a grant from the University of California President's Office through the Campus-Laboratory Collaboration program (K.-I. Chang), by a NSF Special Creativity Award (M. Ghil), by ONR Grant N00014-99-1-0020 (K. Ide), and by a Los Alamos LDRD Project (C. Lai). K.-I. Chang was also partly supported by the Ministry of Maritime Affairs and Fisheries in Korea as part of the research program ''Korea Ocean Prediction System'' under Grant BSPM 99025-00-1216-1. M.G. would like, furthermore, to thank his hosts at the Ecole Normale Supérieure in Paris for their hospitality during the sabbatical that helped complete this work. This is publication number 5482 of the UCLA Institute of Geophysics and Planetary Physics.

REFERENCES

Auer, S. J., 1987: Five-year climatological survey of the Gulf Stream System and its associated rings. *J. Geophys. Res.,* **92,** 11 709–11 726.

Barenblatt, G. L., 1987: *Dimensional Analysis.* Gordon and Breach, 135 pp.

Berloff, P. S., and S. P. Meacham, 1997: The dynamics of an equivalent barotropic model of the wind-driven circulation. *J. Mar. Res.,* **55,** 407–451.

——, and ——, 1998: The dynamics of a simple baroclinic model of the wind-driven circulation. *J. Phys. Oceanogr.,* **28,** 361–388.

——, and J. C. McWilliams, 1999a: Large-scale, low-frequency variability in wind-driven ocean gyres. *J. Phys. Oceanogr.,* **29,** 1925–1949.

——, and ——, 1999b: Quasigeostrophic dynamics of the western boundary current. *J. Phys. Oceanogr.,* **29,** 2607–2634.

Böning, C. W., 1986: On the influence of frictional parameterization in wind-driven ocean circulation models. *Dyn. Atmos. Oceans,* **10,** 63–92.

Briggs, W. L., 1980: A new class of steady solutions of the barotropic vorticity equation. *Dyn. Atmos. Oceans,* **4,** 67–99.

Brugge, B., 1995: Near surface mean circulation and eddy kinetic energy in the central North Atlantic from drifter data. *J. Geophys. Res.,* **100,** 20 543–20 554.

Bryan, K., 1963: A numerical investigation of a nonlinear model of a wind-driven ocean. *J. Atmos. Sci.,* **20,** 594–606.

Cessi, P., and G. R. Ierley, 1995: Symmetry-breaking multiple equilibria in quasi-geostrophic, wind-driven flows. *J. Phys. Oceanogr.,* **25,** 1196–1205.

Chao, Y., A. Gangopadhyay, F. O. Bryan, and W. R. Holland, 1996: Modeling the Gulf Stream system: How far from reality? *Geophys. Res. Lett.,* **23,** 3155–3158.

Chassignet, E. P., and Coauthors, 2000: DAMEE-NAB: The base experiments. *Dyn. Atmos. Oceans,* **32,** 155–183.

Chen, F., and M. Ghil, 1996: Interdecadal variability in a hybrid coupled ocean–atmosphere model. *J. Phys. Oceanogr.,* **26,** 1561–1578.

Chen, H.-T., X.-H. Han, P.-T. Shaw, and Q. Zheng, 1996: A numerical simulation of wind stress and topographic effects on the Kuroshio current path near Taiwan. *J. Phys. Oceanogr.,* **26,** 1769–1802.

Delworth, T., S. Manabe, and R. J. Stouffer, 1993: Interdecadal variations of the thermohaline circulation in a coupled ocean–atmosphere model. *J. Climate,* **6,** 1993–2011.

Deser, C., M. A. Alexander, and C. A. Timlin, 1996: Upper-ocean thermal variations in the North Pacific during 1970–1991. *J. Climate,* **9,** 1840–1855.

Dettinger, M. D., M. Ghil, C. M. Strong, W. Weibel, and P. Yiou, 1995: Software expedites singular-spectrum analysis of noisy time series. *Eos, Trans. Amer. Geophys. Union,* **76,** pp. 12, 14, and 21.

Dijkstra, H. A., and C. A. Katsman, 1997: Temporal variability of the wind-driven quasi-geostrophic double gyre ocean circulation: Basic bifurcation diagrams. *Geophys. Astrophys. Fluid Dyn.,* **85,** 195–232.

——, and M. J. Molemaker, 1999: Imperfections of the North Atlantic wind-driven ocean circulation: Continental geometry and wind stress. *J. Mar. Res.,* **57,** 1–28.

Fu, L.-L., and R. D. Smith, 1996: Global ocean circulation from satellite altimetry and high-resolution computer simulation. *Bull. Amer. Meteor. Soc.,* **77,** 2625–2636.

Gawarkiewicz, G., and D. C. Chapman, 1991: Formation and maintenance of shelfbreak fronts in an unstratified flow. *J. Phys. Oceanogr.,* **21,** 1225–1239.

Ghil, M., and S. Childress, 1987: *Topics in Geophysical Fluid Dy-*

namics: Atmospheric Dynamics, Dynamo Theory and Climate Dynamics. Springer-Verlag, 485 pp.

——, and A. W. Robertson, 2000: Solving problems with GCMs: General circulation models and their role in the climate modeling hierarchy. *General Circulation Model Development: Past, Present, and Future*, D. Randall, Ed., Academic Press, 285–325.

Guckenheimer, I., and P. Holmes, 1983: *Nonlinear Oscillations, Dynamical Systems and Bifurcations of Vector Fields*. Springer-Verlag, 453 pp.

Haidvogel, D. B., J. L. Wilkin, and R. Young, 1991a: A semi-spectral primitive equation ocean circulation model using vertical sigma and orthogonal curvilinear horizontal coordinates. *J. Comput. Phys.*, **94,** 151–185.

——, A. Beckmann, and K. S. Hedstrom, 1991b: Dynamical simulations of filament formation and evolution in the Coastal Transition Zone. *J. Geophys. Res.*, **96,** 15 017–15 040.

——, J. C. McWilliams, and P. R. Gent, 1992: Boundary current separation in a quasigeostrophic, eddy-resolving ocean circulation model. *J. Phys. Oceanogr.*, **22,** 882–902.

Halkin, D., and H. T. Rossby, 1985: The structure and transport of the Gulf Stream at 73° W. *J. Phys. Oceanogr.*, **15,** 1439–1452.

Hall, M. M., 1986: Horizontal and vertical structure of the Gulf Stream velocity field. *J. Phys. Oceanogr.*, **16,** 1814–1828.

Hedstrom, K. S., 1994: User's manual for a semi-spectral primitive equation ocean circulation model, version 3.9. Institute of Marine and Coastal Sciences, Rutgers University, The State University of New Jersey, 131 pp. [Available online at http://www.marine.rutgers.edu/po/.]

Ichikawa, H., and R. C. Beardsley, 1993: Temporal and spatial variability of volume transport of the Kuroshio in the East China Sea. *Deep-Sea Res.*, **40,** 583–605.

Ierley, G. R., and W. R. Young, 1991: Viscous instabilities in the western boundary layer. *J. Phys. Oceanogr.*, **21,** 1323–1332.

——, and V. A. Sheremet, 1995: Multiple solutions and advection-dominated flows in the wind-driven circulation. Part I: Slip. *J. Mar. Res.*, **53,** 703–737.

Jiang, S., and M. Ghil, 1997: Tracking nonlinear solutions with simulated altimetric data in a shallow-water model. *J. Phys. Oceanogr.*, **27,** 72–95.

——, F.-F. Jin, and M. Ghil, 1995: Multiple equilibria, periodic, and aperiodic solutions in a wind-driven, double-gyre, shallow-water model. *J. Phys. Oceanogr.*, **25,** 764–786.

Kamenkovich, V. M., V. A. Sheremet, A. R. Pastushkov, and S. O. Belotserkovsky, 1995: Analysis of the barotropic model of the subtropical gyre in the ocean for finite Reynolds numbers. Part I. *J. Mar. Res.*, **53,** 959–994.

Latif, M., and T. P. Barnett, 1994: Causes of decadal climate variability over the North Pacific and North America. *Science*, **266,** 634–637.

Lee, T., and P. Cornillon, 1996: Propagation and growth rate of Gulf Stream meanders between 75° and 45°W. *J. Phys. Oceanogr.*, **26,** 225–241.

McCalpin, J., and D. B. Haidvogel, 1996: Phenomenology of the low-frequency variability in a reduced-gravity, quasigeostrophic double-gyre model. *J. Phys. Oceanogr.*, **26,** 739–752.

Meacham, S. P., and P. S. Berloff, 1997a: Barotropic, wind-driven circulation in a small basin. *J. Mar. Res.*, **55,** 523–563.

——, and ——, 1997b: Instabilities of a steady, barotropic, wind-driven circulation. *J. Mar. Res.*, **55,** 885–913.

Mizuno, S., and W. B. White, 1983: Annual and interannual variability in the Kuroshio Current System. *J. Phys. Oceanogr.*, **13,** 1847–1867.

Moro, B., 1988: On the non-linear Munk model. I: Steady flows. *Dyn. Atmos. Oceans*, **12,** 259–288.

——, 1990: On the non-linear Munk model. II: Stability. *Dyn. Atmos. Oceans*, **14,** 203–227.

Moron, V., R. Vautard, and M. Ghil, 1998: Trends, interdecadal and interannual oscillations in global sea-surface temperatures. *Climate Dyn.*, **14,** 545–569.

Munk, W. H., 1950: On the wind-driven ocean circulation. *J. Meteor.*, **7,** 79–93.

Niiler, P. P., and W. S. Richardson, 1973: Seasonal variability of the Florida Current. *J. Mar. Res.*, **31,** 144–167.

Olson, D., G. Podesta, R. Evans, and O. Brown, 1988: Temporal variations in the separation of Brazil and Malvinas Currents. *Deep-Sea Res.*, **35,** 1971–1980.

Pedlosky, J., 1996: *Ocean Circulation Theory*. Springer-Verlag, 453 pp.

Primeau, F. W., 1998: Multiple equilibria of a double-gyre ocean model with super-slip boundary conditions. *J. Phys. Oceanogr.*, **28,** 2130–2147.

Quon, C., and M. Ghil, 1992: Multiple equilibria in thermosolutal convection due to salt-flux boundary conditions. *J. Fluid Mech.*, **245,** 449–483.

——, and ——, 1995: Multiple equilibria and stable oscillations in thermosolutal convection at small aspect ratio. *J. Fluid Mech.*, **291,** 33–56.

Robertson, A. W., 1996: Interdecadal variability in a multicentury climate integration. *Climate Dyn.*, **12,** 227–241.

Schott, F., and R. L. Molinari, 1996: The western boundary circulation of the subtropical warmwatersphere. *The Warm Water Sphere of the North Atlantic Ocean*, W. Krauss, Ed., Gebrüder Borntraeger, 229–252.

Sheremet, V. A., V. M. Kamenkovich, and A. R. Pastushkov, 1995: Analysis of the barotropic model of the subtropical gyre in the ocean for finite Reynolds numbers. Part II. *J. Mar. Res.*, **53,** 995–1024.

——, G. R. Ierley, and V. M. Kamenkovich, 1997: Eigenanalysis of the two-dimensional wind-driven ocean circulation problem. *J. Mar. Res.*, **55,** 57–92.

Simonnet, E., 1998: Quelques problèmes numérique associés aux ecoulements géophysiques. Ph.D. thesis, University of Paris-Sud, Orsay, France, 150 pp. [Available online at http://www.atmos.ucla.edu/tcd/.]

Speich, S., H. Dijkstra, and M. Ghil, 1995: Successive bifurcations in a shallow-water model applied to the wind-driven ocean circulation. *Nonlinear Proc. Geophys.*, **2,** 241–268.

Stommel, H., 1948: The westward intensification of wind-driven ocean currents. *Trans. Amer. Geophys. Union*, **29,** 202–206.

Témam, R., 1997: *Infinite-Dimensional Dynamical Systems in Mechanics and Physics*. Springer-Verlag, 648 pp.

Veronis, G., 1963: An analysis of wind-driven ocean circulation with a limited number of Fourier components. *J. Atmos. Sci.*, **20,** 577–593.

——, 1966: Wind-driven ocean circulation. Part II. *Deep-Sea Res.*, **13,** 30–55.

Wyrtki, K., L. Magaard, and J. Hagger, 1976: Eddy energy in the oceans. *J. Geophys. Res.*, **81,** 2641–2646.